



Spray Chemical Vapor Deposition of Single-Source Precursors for Chalcopyrite I-III-VI₂ Thin-Film Materials

Aloysius F. Hepp
Glenn Research Center, Cleveland, Ohio

Kulbinder K. Banger
Ohio Aerospace Institute, Cleveland, Ohio

Michael H.-C. Jin
University of Texas at Arlington, Arlington, Texas

Jerry D. Harris
Northwest Nazarene University, Nampa, Idaho

Jeremiah S. McNatt and John E. Dickman
Glenn Research Center, Cleveland, Ohio

NASA STI Program . . . in Profile

Since its founding, NASA has been dedicated to the advancement of aeronautics and space science. The NASA Scientific and Technical Information (STI) program plays a key part in helping NASA maintain this important role.

The NASA STI Program operates under the auspices of the Agency Chief Information Officer. It collects, organizes, provides for archiving, and disseminates NASA's STI. The NASA STI program provides access to the NASA Aeronautics and Space Database and its public interface, the NASA Technical Reports Server, thus providing one of the largest collections of aeronautical and space science STI in the world. Results are published in both non-NASA channels and by NASA in the NASA STI Report Series, which includes the following report types:

- **TECHNICAL PUBLICATION.** Reports of completed research or a major significant phase of research that present the results of NASA programs and include extensive data or theoretical analysis. Includes compilations of significant scientific and technical data and information deemed to be of continuing reference value. NASA counterpart of peer-reviewed formal professional papers but has less stringent limitations on manuscript length and extent of graphic presentations.
- **TECHNICAL MEMORANDUM.** Scientific and technical findings that are preliminary or of specialized interest, e.g., quick release reports, working papers, and bibliographies that contain minimal annotation. Does not contain extensive analysis.
- **CONTRACTOR REPORT.** Scientific and technical findings by NASA-sponsored contractors and grantees.
- **CONFERENCE PUBLICATION.** Collected

papers from scientific and technical conferences, symposia, seminars, or other meetings sponsored or cosponsored by NASA.

- **SPECIAL PUBLICATION.** Scientific, technical, or historical information from NASA programs, projects, and missions, often concerned with subjects having substantial public interest.
- **TECHNICAL TRANSLATION.** English-language translations of foreign scientific and technical material pertinent to NASA's mission.

Specialized services also include creating custom thesauri, building customized databases, organizing and publishing research results.

For more information about the NASA STI program, see the following:

- Access the NASA STI program home page at <http://www.sti.nasa.gov>
- E-mail your question via the Internet to help@sti.nasa.gov
- Fax your question to the NASA STI Help Desk at 301-621-0134
- Telephone the NASA STI Help Desk at 301-621-0390
- Write to:
NASA Center for AeroSpace Information (CASI)
7115 Standard Drive
Hanover, MD 21076-1320



Spray Chemical Vapor Deposition of Single-Source Precursors for Chalcopyrite I-III-VI₂ Thin-Film Materials

Aloysius F. Hepp
Glenn Research Center, Cleveland, Ohio

Kulbinder K. Banger
Ohio Aerospace Institute, Cleveland, Ohio

Michael H.-C. Jin
University of Texas at Arlington, Arlington, Texas

Jerry D. Harris
Northwest Nazarene University, Nampa, Idaho

Jeremiah S. McNatt and John E. Dickman
Glenn Research Center, Cleveland, Ohio

National Aeronautics and
Space Administration

Glenn Research Center
Cleveland, Ohio 44135

Acknowledgments

The authors gratefully acknowledge NASA for financial support through cooperative agreement NCC3-947 and NCC04AA71A. We also wish to thank Mr. David Scheiman from the Ohio Aerospace Institute for his assistance with the solar simulator at NASA Glenn Research Center and Mr. Philip Jenkins also from the Ohio Aerospace Institute for his assistance with the photoluminescence measurements. We are grateful to Dr. Robert Birkmire, Dr. William Shafarman, and the staff at the Institute of Energy Conversion of the University of Delaware for their help with solar cell fabrication. We also acknowledge the contributions of Drs. William Buhro and Jennifer Hollingsworth from Washington University, Dr. John Scofield from Oberlin College, and Mr. Jonathan Cowen from Case Western Reserve University. Finally, we acknowledge Dr. Kannan Ramanathan of the National Renewable Energy Laboratory for providing a shadow mask.

Trade names and trademarks are used in this report for identification only. Their usage does not constitute an official endorsement, either expressed or implied, by the National Aeronautics and Space Administration.

Level of Review: This material has been technically reviewed by an expert single reviewer.

Available from

NASA Center for Aerospace Information
7115 Standard Drive
Hanover, MD 21076-1320

National Technical Information Service
5285 Port Royal Road
Springfield, VA 22161

Available electronically at <http://gltrs.grc.nasa.gov>

Spray Chemical Vapor Deposition of Single-Source Precursors for Chalcopyrite I-III-VI₂ Thin-Film Materials

Aloysius F. Hepp
National Aeronautics and Space Administration
Glenn Research Center
Cleveland, Ohio 44135

Kulbinder K. Banger
Ohio Aerospace Institute
Cleveland, Ohio 44142

Michael H.-C. Jin
University of Texas at Arlington
Arlington, Texas 76019

Jerry D. Harris
Northwest Nazarene University
Nampa, Idaho 83686

Jeremiah S. McNatt and John E. Dickman
National Aeronautics and Space Administration
Glenn Research Center
Cleveland, Ohio 44135

Summary

Thin-film solar cells on flexible lightweight space-qualified substrates provide an attractive approach to fabricating solar arrays with high mass-specific power. A polycrystalline chalcopyrite absorber layer is among the new generation of photovoltaic device technologies for thin-film solar cells. At NASA Glenn Research Center we have focused on the development of new single-source precursors (SSPs) for deposition of semiconducting chalcopyrite materials onto lightweight, flexible substrates. We describe the syntheses and thermal modulation of SSPs via molecular engineering. Copper indium disulfide and related thin-film materials were deposited via aerosol-assisted chemical vapor deposition using SSPs. Processing and post-processing parameters were varied in order to modify morphology, stoichiometry, crystallography, electrical properties, and optical properties to optimize device quality. Growth at atmospheric pressure in a horizontal hot-wall reactor at 395 °C yielded the best device films. Placing the susceptor closer to the evaporation zone and flowing a more precursor-rich carrier gas through the reactor yielded shinier, smoother, denser looking films. Growth of (112)-oriented films yielded more Cu-rich films with fewer secondary phases than growth of (204)/(220)-oriented films. Post deposition sulfur-vapor annealing enhanced the stoichiometry and crystallinity of films. Photoluminescence studies revealed four major emission bands and a broad band associated with deep defects. The highest device efficiency for a chemical-vapor-deposited cell was 1 percent.

Introduction

The development of new technologies that will enable the exploration of the universe has been one of the major goals of NASA since its founding in 1958. New power technologies will enhance the performance of rovers, satellites, and other payloads as the Agency advances its broad-based charter in aeronautics and space exploration.

With the increasing cost of launching payloads into space—currently estimated to be approximately \$20,000 per kilogram—lightweight materials for space power systems are now being considered. Use of solar cells that are flexible (fig. 1), which allows for their efficient storage in launch vehicles for later controlled deployment in space, will enable several proposed NASA space missions.

As part of its efforts to fulfill these goals, NASA Glenn Research Center has been working to develop novel fabrication technologies to enable deployment of lightweight thin-film solar cells for space power generation (refs. 1 to 9). The ability to deposit thin films on lightweight flexible substrates will lead to more design flexibility and lower launch costs as well as provide extra space and mass for payloads.

In fact, the development of thin-film flexible lightweight solar cells is important for both terrestrial and space applications. Thin-film solar cells use 30 to 100 times semiconducting material and are less expensive to manufacture than conventional crystalline silicon cells. For many terrestrial applications, thin-film photovoltaic (PV) technologies are advantageous because of their flexible

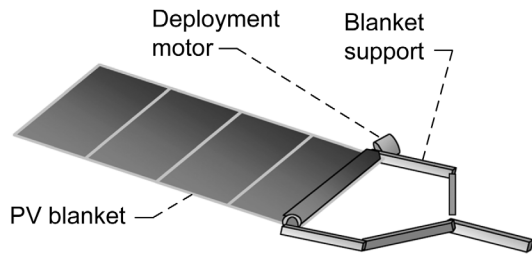


Figure 1.—Lightweight flexible photovoltaic (PV) array.

lightweight construction, permitting them to be “molded” onto nonrigid, or uniform structures for innovative power systems. Importantly for space applications, their lightweight structure enables them to achieve much higher mass specific power (W/kg) than conventional single-crystalline device technologies (ref. 10).

Current thin-film PV research encompasses development of CdTe, Cu(In,Ga)(S,Se)₂ (CIGSSe), and thin-film silicon-based solar cells (ref. 11). PV devices based on the family of chalcopyrite absorber layers I-III-VI₂ or CIGSSe have been the particular focus of intense investigation for over two decades. The use of chalcopyrite absorbers is quite advantageous since the bandgaps of many of these alloys are a good match for the maximum photon power density in the solar spectrum for both terrestrial (AM1.5), and space applications (AM0) (fig. 2), while displaying long-term stability and excellent radiation tolerance (refs. 12 to 14). Additionally, by adjusting the percent (atomic) composition of either Ga for In and/or S for Se, the bandgap can be tuned from 1.0 to 2.4 eV, thus permitting fabrication of high or graded bandgaps (ref. 15).

Polycrystalline CuInS₂ was chosen as the target absorber layer for the effort at NASA Glenn because of its high absorption coefficient and its direct bandgap of 1.5 eV, which is near optimum for AM0 conditions. The CuInS₂ films typically occur in either a sphalerite (more disordered) or a chalcopyrite structure, which is preferred in solar cells for PV applications. So far, the highest total area efficiency achieved by a CuInS₂ cell using vacuum-based co-evaporation techniques has been 12.5 percent (ref. 16). Other alloys of CIGSSe, such as Cu(In,Ga)Se₂ (CIGS), have shown conversion efficiencies of as high as 19.2 percent under AM1.5 illumination (ref. 17). However, the 1.5 eV direct bandgap of CuInS₂ makes it ideal for solar radiation conversion in space. Also, CuInS₂ thin films are more resistant to radiation in space than other CIGS alloys (refs. 12 and 13); thus, they can be used as a top cell in a tandem structure with CIGS (ref. 18), and they are less toxic to process than selenium-containing alloys.

A key technical issue outlined in the 2001 U.S. Photovoltaic Industry Roadmap (ref. 19) is the need to develop low-cost high-throughput manufacturing for high-

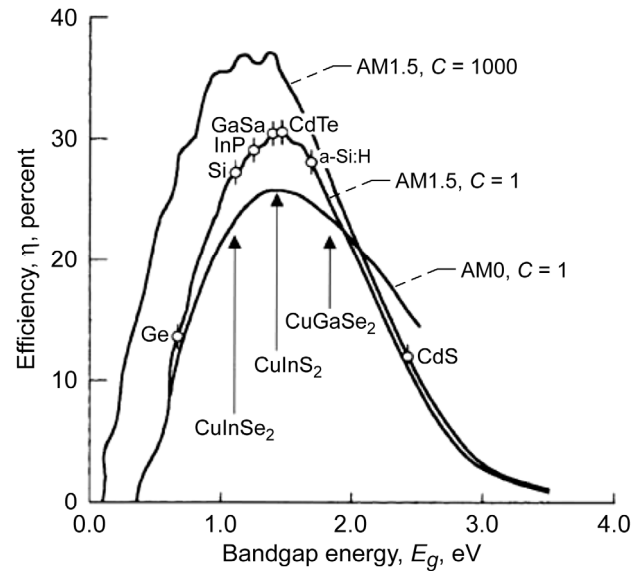


Figure 2.—Predicted efficiency versus bandgap for thin-film photovoltaic materials for solar spectrum in space (AM0, air mass zero) and on the surface of the Earth (AM1.5) at 300 K compared with bandgaps of other materials with unconcentrated ($C = 1$) and high concentration ($C = 1000$) sunlight.

efficiency thin-film solar cells. Thus, an important process to target for device fabrication for thin-film solar cells is deposition onto flexible lightweight substrates such as polyimides. Current methods for depositing ternary polycrystalline compounds include co-evaporation of elements (refs. 20 to 22) or alloys (ref. 23), electrodeposition (ref. 24), reactive-sintering (ref. 25), and flash evaporation (ref. 26), which are often followed by toxic sulphurization or selenization steps at elevated temperatures. Furthermore, under these conditions loss of volatile In/Ga chalcogenides is common (refs. 20 and 27). The high temperature requirements make this protocol incompatible with all presently known flexible polyimides or other polymer substrates. In addition, the use of toxic reagents is a limiting factor. The use of multisource inorganic or organometallic precursors in a type of chemical vapor deposition (CVD) process is more appealing because of milder process parameters. However, stoichiometric control of deposited films can be difficult to achieve, and film contamination has been reported (refs. 28 and 29).

A novel alternative approach is the use of ternary single-source precursors, (SSPs), which have the I-III-VI₂ stoichiometry “built in” and are suitable for low-temperature deposition (fig. 3). Although a rich and diverse array of binary SSPs are known (refs. 30 to 34) and have been characterized, reviewed, and tested, the number of known ternary SSPs is limited, as is their use in deposition processes (ref. 30). SSPs for chalcopyrite (I-III-VI₂) materials possibly offer a cleaner or

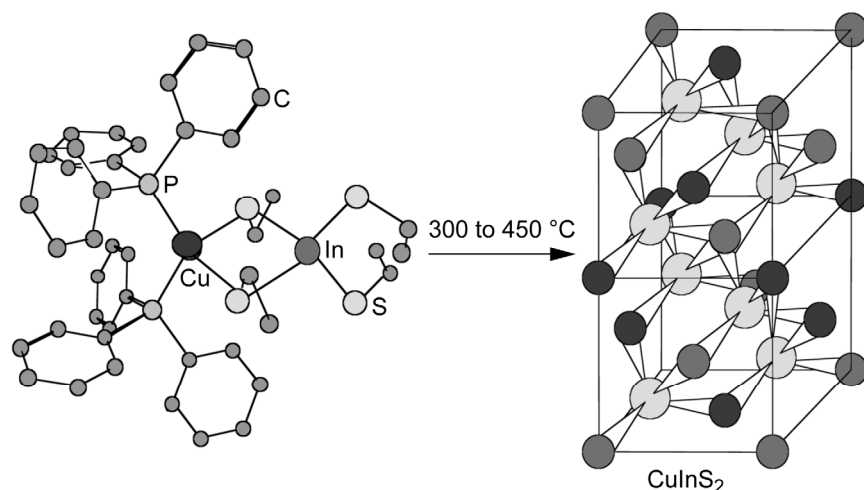


Figure 3.—Example of pyrolysis of $[\{\text{PPh}_3\}_2\text{Cu}(\mu\text{-SEt})_2\text{In}(\text{SEt})_2]$ (precursor 1 in table I) to produce semiconductor CuInS_2 .

“greener” approach for depositing thin films. One advantage is that they offer a number of tunable sites within the complex, allowing various combinations for depositing chalcopyrite films of different compositions. Early work on SSPs was performed by Nomura (refs. 35 to 38) and Kanatzidis (ref. 39). Buhro and Hepp later demonstrated that the thiolate-bridged bimetallic complex, $[\{\text{PPh}_3\}_2\text{Cu}(\mu\text{-SEt})_2\text{In}(\text{SEt})_2]$, could be used in a spray CVD process for depositing CuInS_2 thin films, with processing temperatures under 400°C (refs. 40 to 42). A review of work on chemical precursors was recently reported (ref. 3).

Films at NASA Glenn were deposited using homemade spray or aerosol-assisted CVD (AACVD) reactors to exploit the lower deposition temperature enabled by the simpler decomposition chemistry for the SSPs (refs. 6 to 9). AACVD itself is a simple and inexpensive process that offers the advantage of a uniform, large-area deposition, just like metal organic CVD (MOCVD), while also offering the low-temperature solution reservoir typical of spray pyrolysis methods.

Following growth of films and completion of devices, characterization techniques were employed to determine the properties and performances of the films and devices. Film thicknesses were measured using a profilometer (Sloan Dektak IIA or KLA-Tencor HRP 75). Film morphologies were studied using scanning electron microscopy (SEM) (Hitachi S-3000N and S-800). The Hitachi S-3000N includes a built-in energy dispersive spectroscopy (EDS) system (EDAX Falcon) used to examine film compositions. Compositional measurements were performed in different areas across each cell in order to determine the compositional uniformity. The Cu/In ratios were obtained by quantifying the Cu K_α and In L emission lines using the ZAF standardless method. X-ray diffraction (XRD) (PANalytical X’pert Pro) was used in order to identify the phases, and glancing angle XRD (GAXRD) was performed using the same instrument to identify the phases present at the

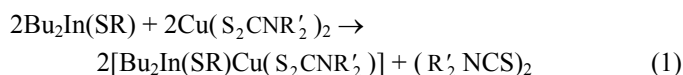
film surfaces. The optical bandgaps of the films were determined by analyzing transmittance measurements taken in a UV/VIS spectrophotometer (PerkinElmer Lambda 19). Electrical measurements were performed using a four-point probe system (a Bio-Rad Laboratories HL5500PC) operated in the van der Pauw configuration, and a custom hot-point probe system—a Weller TC201 soldering iron (Cooper Industries, LLC)—was used as the hot probe.

Throughout the NASA Glenn studies, various processing and postprocessing parameters were modified in order to determine how they affected morphology, stoichiometry, crystallography, electrical properties, and optical properties of the deposited thin films. Some of the modifications made included varying the reactor type and configuration, deposition temperatures, location of the substrate within the reactor, annealing times, and annealing atmospheres. We will discuss several deposition designs and details of processing experiments and their impact on film properties. Complete working devices were also fabricated and tested. Hence, it is the goal of this review to highlight recent advances from NASA Glenn and other groups, summarizing the current state of the art of this highly promising technique for thin-film growth, exploiting molecular design of SSPs and monitoring film quality as it relates to and is predictive of device performance.

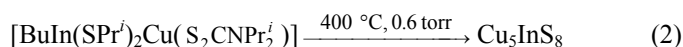
Single-Source Precursor (SSP) Studies

In early studies, Nomura et al. reported that an equimolar mixture of Bu_2InSP^n and $\text{Cu}(\text{S}_2\text{CNBu}_2)_2$ decomposed to afford CuInS_2 powders (ref. 35). Solution pyrolysis of this mixture dissolved in *p*-xylene was used to deposit thin-film CuInS_2 at 350°C onto glass substrates. Film composition, analyzed by EDS, revealed that the ratios of In/Cu and S/Cu

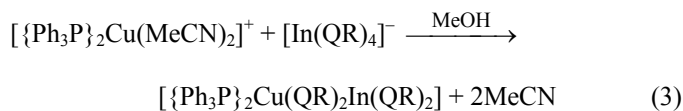
decreased with substrate temperature, and XRD showed that a second phase was present for films deposited at 350 °C. Grain size was estimated to be in the range of 50 to 100 nm as determined by SEM. It was later realized that the equimolar reaction mixture of $[\text{Bu}_2^i\text{In}(\text{SPr}^n)]$ and $[\text{Cu}(\text{S}_2\text{CNBu}_2^n)_2]$ (as used in solution pyrolysis) afforded the SSP $[\text{Bu}_2^i\text{In}(\text{SPr}^n)\text{Cu}(\text{S}_2\text{CNBu}_2^n)]$ before decomposing to the chalcopyrite matrix (see eq. (1)) (ref. 36). Analytical and spectral data confirmed that the mixture of $[\text{Bu}_2^i\text{In}(\text{SPr}^n)]$ and $[\text{Cu}(\text{S}_2\text{CNBu}_2^n)_2]$ yielded a SSP, although the nature of the chemical bridge was not well defined. Other analogous ternary CuInS_2 precursors were also synthesized by the reaction of alkyl indium thiolates with copper dithiocarbamates (ref. 37). However, only $[\text{Bu}_2\text{In}(\text{SPr}^i)\text{Cu}(\text{S}_2\text{CNPr}_2^i)]$ was successfully implemented for depositing pure CuInS_2 by low-pressure MOCVD. In the case of $[\text{BuIn}(\text{SPr}^i)\text{Cu}(\text{S}_2\text{CNPr}_2^i)]$, tetragonal CuIn_5S_8 was deposited (i.e., see eq. (2)) (ref. 38):



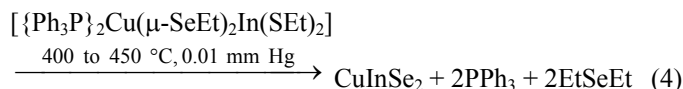
where either $\text{R} = \text{Pr}^n$ and $\text{R}' = \text{Bu}^n$ or $\text{R} = \text{R}' = \text{Pr}^i$



Several years later, Kanatzidis et al. reported the preparation of heterobinuclear complexes of tetrahedrally arranged Cu and In centers with two bridging thiolato or selenolato groups, $[\{\text{PPh}_3\}_2\text{Cu}(\mu\text{-QEt})_2\text{In}(\text{SEt}_2)]$, ($\text{Q} = \text{S}$ or Se) (ref. 39). Hereafter the symbol μ indicating a bridging geometry will be eliminated for the sake of simplicity and clarity. Pyrolysis studies undertaken revealed that the Se derivative could be converted to CuInSe_2 at 400 to 450 °C and 0.01 mm Hg (eqs. (3) and (4)). However, none of the precursors had been evaluated in a thin-film deposition study.



where $\text{R} = \text{Et}$ or Bu^i



In continuing the NASA-funded work, Buhro and Hepp were able to demonstrate that In and Cu binuclear thiolato or selenolato complexes could be utilized in a spray CVD process for depositing thin-film CuInS_2 below 400 °C (refs. 40 to 42). Thin films were deposited using a dual solvent system of toluene and dichloromethane as the carrier solvent. Single-phase (112)-oriented CuInS_2 films were successfully deposited at a range of temperatures from 300 to 400 °C, while CuIn_5S_8 -phase films could be deposited at elevated temperatures (>500 °C). Rutherford backscattering spectroscopy, EDS, and x-ray photoelectron spectroscopy analyses showed that the films were free from any detectable impurities and highly crystalline, thus concluding that the precursor decomposes cleanly. During the course of the study, the morphology of the deposited films were found to be temperature and carrier solvent dependent. Films deposited at 300 and 350 °C yielded a grain size of 400 to 800 nm, with smaller, finer particles of 50 to 200 nm resident on top. At a higher deposition temperature of 400 °C, the films consisted of more angular grains and a more uniform grain size of approximately 200 to 400 nm. Photoluminescence (PL) data and optical transmission measurements confirmed that the deposited CuInS_2 thin films were direct bandgap semiconductors.

In the course of our investigations for improved SSPs for the spray CVD of CIGSSe chalcopyrite thin films, we have continued to expand the molecular design of SSPs based on the $[\{\text{ER}_3\}_2\text{Cu}(\text{QR}')_2\text{M}(\text{QR}')_2]$ architecture (ref. 39). Furthermore, the number of “tunable” sites within the complex allows for their utility in preparing a number of ternary chalcopyrites of varying composition, in addition to engineering the SSP to match a given spray CVD process (fig. 4).

Chemical Synthesis of SSPs

The SSPs are prepared by the reaction of a stabilized Cu(I) cation with an In(III) or Ga(III) chalcogenide anion, prepared in situ by reaction of the conjugate acid of the thiol or selenol with NaOMe in methanol (refs. 1 and 3). Scheme 1 in figure 5 illustrates the synthesis of a CuInQ_2 precursor.

The versatility of this synthetic pathway is illustrated by the ability to modulate the physical properties of the precursor and its stoichiometry at any of the intermediate synthetic steps by

- (1) Adjusting the Lewis acid-base interaction ($\text{E} \rightarrow \text{M}$, $\text{M} =$ group 11 metal)
- (2) Adjusting the accessibility of the lone pair of electrons on the neutral donor ligand by variation of R
- (3) Adjusting the bond strength between the chalcogenide with either indium or gallium and copper metal centers

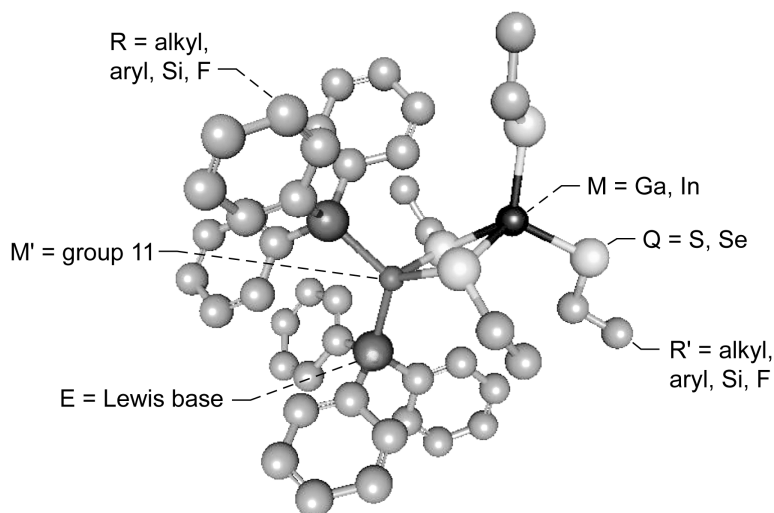


Figure 4.—Molecular structure diagram of $[[\text{PPH}_3]_2\text{Cu}(\text{SET})_2\text{In}(\text{SET})_2]$ (precursor **1** in table I), indicating tunable sites of $[[\text{ER}_3]_2\text{M}'(\text{QR}')_2\text{M}(\text{QR}')_2]$ architecture.

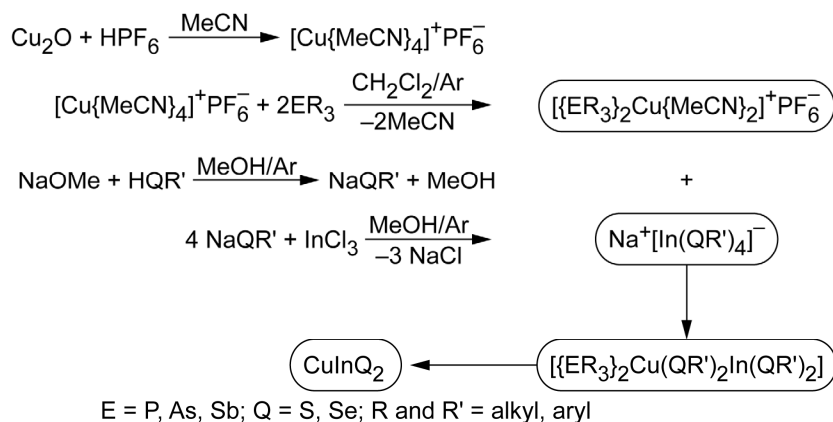


Figure 5.—Scheme 1: Synthesis of ternary SSPs and subsequent production of I–III–VI₂ material.

- (4) Changing the precursor composition using either sulfur or selenium moieties
- (5) Changing the precursor composition using either indium or gallium moieties

The Lewis acid-base interaction is a valuable component to the overall stability of the molecule, given that the ability of the Lewis base to dissociate from the cation at lower energies is pertinent to the degradation of the precursor at reduced temperatures. Hence, the Drago-Wayland approximation (ref. 43) can be used for ternary SSP design, to quantitatively estimate the strength of the Lewis acid-base interaction between the copper center and the neutral donor. The cleavage of chalcogenide–R' bonds also plays an important role, since this allows the chalcogenide to be released for incorporation into the ternary chalcopyrite matrix. Hence, the use of a sterically demanding R' group of good “leaving ability” would promote the facile release of the chalcogenide.

Thermal Analysis and Characterization of SSPs

Initial studies focused on basic modification of the SSPs and their influence on precursor stability. Multinuclear nuclear magnetic resonance (NMR) data demonstrated that the precursors were free from any starting reagents. Thermogravimetric analyses (TGA) were performed at ambient pressure on samples of the precursors in platinum pans heated at a rate of 10 °C/min under a nitrogen atmosphere (fig. 6). Weight loss was associated with decomposition of the complexes. Calculation of the derivative maximum rate of weight loss (%/°C), listed as MRW in table I, shows a range from a low of 225 %/°C for **8** to a high of 325 %/°C for **5**. The measured weight loss, based upon the residual (pyrolysate) material from TGA experiments, was within 5 percent (see fig. 6(a)) of expected total weight loss, assuming complete conversion to CuInS₂ or CuInSe₂.

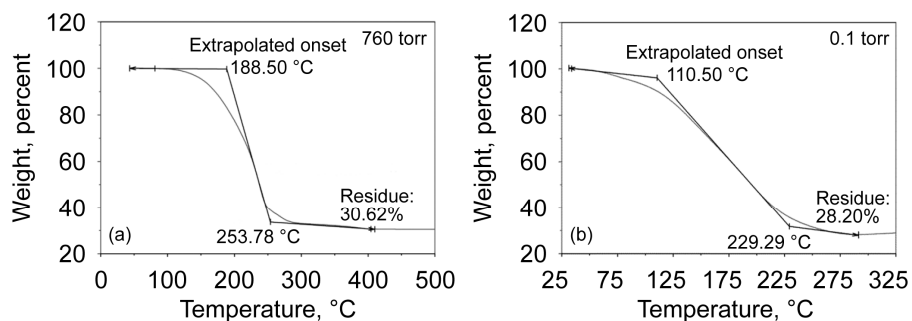


Figure 6.—Thermogravimetric analysis (TGA) profiles at different pressures for $[\{PBU_3\}_2Cu(SEt)_2In(SEt)_2]$ (precursor **7** in table I). (a) 760 torr. (b) 0.1 torr.

A further example of the flexibility of the $[\{ER_3\}_2Cu(QR')_2M(QR')_2]$ architecture to direct adjustment of these precursors are the SSPs **7** and **8**, which represent the first liquid single-source precursors for the deposition of $CuInS_2$ (ref. 1). Added benefits of a charge-neutral liquid precursor are the potential for greater solubility in nonpolar organic solvents and direct delivery without the need for a carrier solvent. Both these enhancements permit the use of higher molarity solutions, which can help achieve thicker $CuInS_2$ thin films without an increase in deposition run times. Because of their semiviscous nature, the physical properties of the clear neat liquid precursors were studied.

Low-temperature differential scanning calorimetry (DSC) was used to investigate the liquid phase of **7** and **8**. In separate studies, samples **7** and **8** were subjected to both quench cooling and slow controlled cooling before being heated at 10 and 5 °C/min (ref. 43). In low-temperature DSC experiments using controlled and quench cooling, both samples **7** and **8** were found not to show an endotherm assignable to a melting phase transition before decomposition, thus supporting their liquid state at ambient temperatures (see fig. 7).

Examination of the other phase transitions reveal the main exothermic events for **7** and **8** begin with extrapolated onset temperatures of 262 and 239 °C, respectively, which represent the decomposition of the samples. The lower decomposition temperature of **8** can be explained by the increase in chain length and/or steric “bulk” of the alkyl groups, which is known to decrease the stability of a complex (ref. 30). In addition, preliminary vacuum-TGA studies for the thermal profile for SSP **7** shows the extrapolated onset can be lowered by ~80 °C thus lowering the degradation temperature window and making these precursors highly suitable for use in low-temperature or low-pressure spray CVD on space-qualified substrates such as Kapton (DuPont) (fig. 6(b)). Remarkably, both liquid precursors show excellent solubility in both polar and nonpolar solvents, attributed to their ionic structure and the nonpolar alkyl groups resident on the tertiary phosphine.

The ability of the new precursors to thermally decompose to yield single-phase $CuInS_2$ was investigated by powder XRD analysis and EDS on the nonvolatile solids from the TGA experiments of selected compounds. Furthermore, using

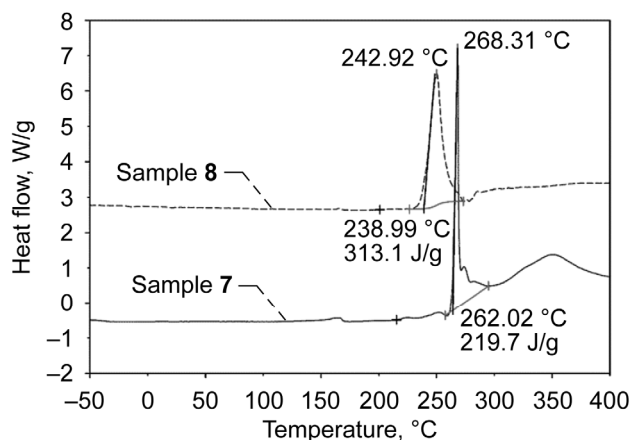


Figure 7.—Low-temperature differential scanning calorimetry (DSC) of $[\{PBU_3\}_2Cu(SEt)_2In(SEt)_2]$ and $[\{PBU_3\}_2Cu(SPr^i)_2In(SPr^i)_2]$ (precursors **7** and **8**, respectively, in table I). Specific heats of phase transitions are indicated in J/g.

TGA–EGA (evolved gas analysis), the volatile components from the degradation of the SSPs could be analyzed via real-time Fourier transform infrared (FTIR) and mass spectrometry (MS), thus providing information for the decomposition mechanism (ref. 35). The real-time FTIR spectra for **7** and **8** show absorptions at approximately 3000, 1460, 1390, 1300, and 1250 cm^{-1} (see fig. 8).

Correlation with the EGA–MS allows for the assignment to the initial loss of diethyl sulfide, as supported by the library fit and from the assignment of the fragment and parent ions (mass-to-charge ratio $m/z = 90$) (see fig. 9(a)). After approximately 15 min, EGA–MS shows the absence of peaks assignable to Et_2S and the occurrence of fragment ions with m/z greater than 90, with an intense peak at $m/z = 202$. These can be assigned to the successive loss of PBU_3 , on the basis of its library fit of 92 percent and assignment of the fragment ions (see fig. 9(b)). Thus, the use of TGA–EGA provides conclusive evidence for the mechanism of decomposition for the single-source precursors to occur via the initial loss of a chalcogenide moiety, followed by loss of the neutral donor ligand.

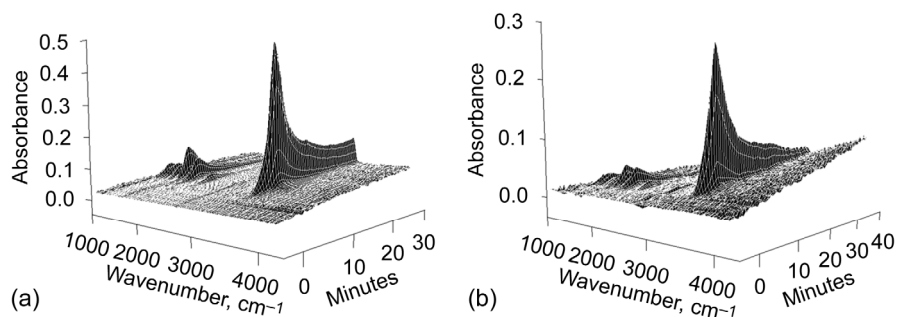


Figure 8.—Evolved gas analysis-Fourier transform infrared (EGA-FTIR) spectra for precursors **7** and **8** in table I. (a) $[\{\text{PBU}_3\}_2\text{Cu}(\text{SEt})_2\text{In}(\text{SEt})_2]$ **7**. (b) $[\{\text{PBU}_3\}_2\text{Cu}(\text{SPr}^n)_2\text{In}(\text{SPr}^n)_2]$ **8**.

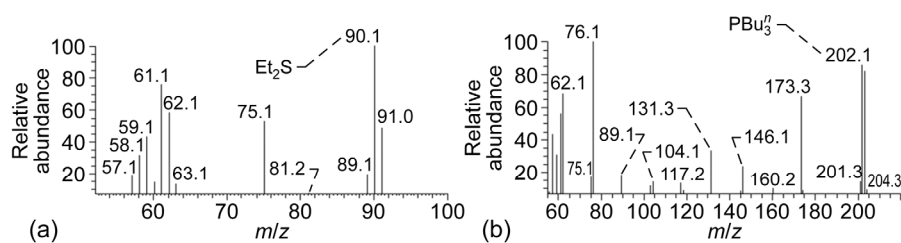


Figure 9.—Evolved gas analysis-mass spectroscopy (EGA-MS, electron impact) data for $[\{\text{PBU}_3\}_2\text{Cu}(\text{SEt})_2\text{In}(\text{SEt})_2]$ (precursor **7** in table I). (a) After ~5 min. (b) After ~15 min.

Preparation of I-III-VI₂ Powders From SSPs

XRD spectra for the nonvolatile material produced from the pyrolysis of **7** (see fig. 10), with the JCPDS reference patterns¹ (ref. 44) for CuInS_2 (27–0159), confirmed it to be single-phase CuInS_2 . Examination of the EDS spectra for the same samples shows predominant emissions due to Cu, In, and S edges, with the approximate percentage atomic composition of 27, 23, and 50 for **7** and 28, 23, and 49 for **8**, thus supporting the formation of CuInS_2 .

The decomposition of the SSP **9** to prepare the semiconductor CuGaS_2 was also investigated (ref. 3). Although the molecular structure for **9** was not fully characterized, its suitability to afford bulk and thin-film CuGaS_2 was studied by TGA (see table I) and XRD. In addition, the optical properties of the deposited thin films were also investigated. Powder XRD analysis on the nonvolatile product from bulk pyrolysis (N_2 , 600 °C) confirmed the collected material to be single-phase (112)-oriented CuGaS_2 (see fig. 11), having an average coherence length of 28 nm.

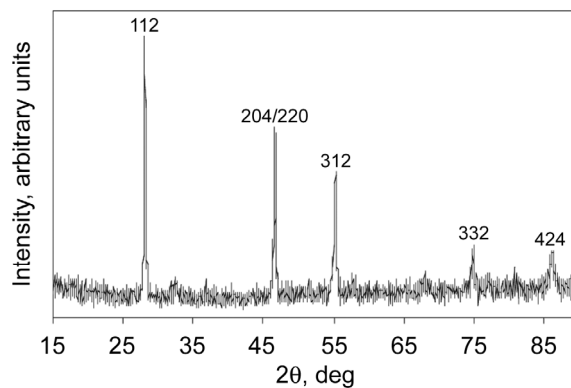


Figure 10.—Powder x-ray diffraction (XRD) pattern ($\text{Cu K}\alpha$, 1.541 Å) for nonvolatile residue from pyrolysis of $[\{\text{PBU}_3\}_2\text{Cu}(\text{SEt})_2\text{In}(\text{SEt})_2]$ (precursor **7** in table I).

¹The Joint Committee on Powder Diffraction Standards (JCPDS) is now the International Center for Diffraction Data (ICDD).

TABLE I.—THERMAL DATA FOR TERNARY SINGLE-SOURCE PRECURSORS (SSPs)

Single-source precursor	Thermogravimetric analysis			Differential scanning calorimetry	
	Extrapolated onset, ^a °C	Maximum rate of weight loss, %/°C	Residue, percent	Melting point, °C	Decomposition temperature, °C
1 [$\{\text{PPh}_3\}_2\text{Cu}(\text{SEt})_2\text{In}(\text{SEt})_2$]	236	269	25	122	266
2 [$\{\text{AsPh}_3\}_2\text{Cu}(\text{SEt})_2\text{In}(\text{SEt})_2$]	205	233	18	47	276
3 [$\{\text{SbPh}_3\}_2\text{Cu}(\text{SEt})_2\text{In}(\text{SEt})_2$]	212	239	26	45	271
4 [$\{\text{PPh}_3\}_2\text{Cu}(\text{SPr}^f)_2\text{In}(\text{SPr}^f)_2$]	215	254	29	163	260
5 [$\{\text{PPh}_3\}_2\text{Cu}(\text{SPh})_2\text{In}(\text{SPh})_2$]	261	325	22	117	280
6 [$\{\text{PPh}_3\}_2\text{Cu}(\text{SePh})_2\text{In}(\text{SePh})_2$]	223	253	22	53	219
7 [$\{\text{PBu}^n_3\}_2\text{Cu}(\text{SEt})_2\text{In}(\text{SEt})_2$]	189	238	31	---	264
8 [$\{\text{PBu}^n_3\}_2\text{Cu}(\text{SPr}^n)_2\text{In}(\text{SPr}^n)_2$]	171	225	29	---	239
9 [$\{\text{PPh}_3\}_2\text{CuGa}(\text{SEt})_x$] ^b	(c)	310	25	(c)	(c)

^aSee figure 5.

^bStructure not elucidated ($x = 3$ or 4).

^cNot recorded.

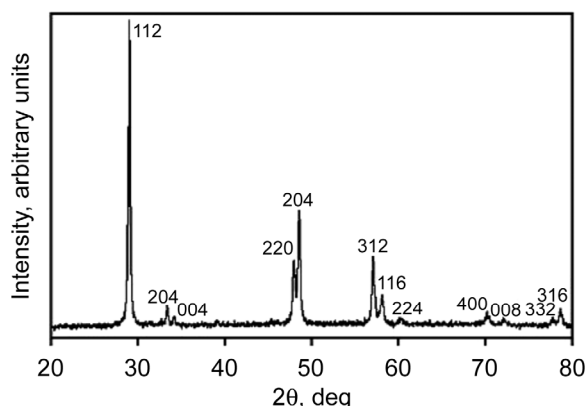


Figure 11.—X-ray diffraction (XRD) pattern of nonvolatile solid obtained from bulk pyrolysis (600 °C, 300 min) of $\{\text{PPh}_3\}_2\text{CuGa}(\text{SEt})_x$ (precursor **9** in table I). All reflections correspond to CuGaS_2 (Power Diffraction File 00–25–0279, ref. 44).

Spray (Aerosol-Assisted) CVD Processing

Spray CVD has become an increasingly popular processing method; a room-temperature precursor solution is ultrasonically nebulized and is swept into a two-zone, hot-wall reactor (see fig. 12(a)). The carrier-solvent is evaporated in the warm zone and the gaseous precursors are decomposed in the hot zone, where film growth occurs, as in conventional CVD. Spray CVD maintains the most desirable features of MOCVD and spray pyrolysis, such as film growth in inert atmospheres, large-area deposition, laminar flow over the substrate, and a low-temperature solution reservoir, while avoiding the major difficulties of each (refs. 45 and 46). It minimizes the high volatility and temperature requirements for the precursor, which are essential in MOCVD, by delivering the precursor to the

furnace as an aerosol propelled by a fast-flowing carrier gas from a low-temperature precursor reservoir analogous to that employed in spray pyrolysis. The latter feature is an important benefit that can prevent premature precursor decomposition when using thermally labile precursors. Most importantly for electronic device growth, the solid-vapor phase interface and precursor decomposition supports the growth of thin films directly rather than allowing growth from intermediate powders or gel films that are more typical of spray pyrolysis processing (ref. 47).

AACVD Reactor Design

Three different reactors were used to deposit CuInS_2 films via aerosol-assisted CVD (AACVD). Reactor A, shown schematically in figure 12(a), was primarily used in the parametric studies described below. This is a horizontal atmospheric-pressure hot-wall reactor with a plate-type 2.5-MHz ultrasonic nebulizer from Sonaer Ultrasonics. The precursor (1.5 to 3.5 g) was dissolved into distilled toluene (50 to 400 ml) and fed into the nebulizer using a syringe pump. The nebulizer created an aerosol that was swept into the reactor by an Ar carrier gas at a flow rate of 4 liter/min (SLPM). The reactor is a two-zone furnace consisting of a warm precursor evaporation zone and a hot deposition zone. The aerosol is converted to precursor vapor and mixes uniformly through the reactor gas in the evaporation zone. A solid graphite susceptor coated with SiC was placed in the deposition zone. The second reactor is a vertical atmospheric-pressure, cold-wall reactor (reactor B, fig. 12(b)) with a commercial ultrasonic nozzle (Sono-Tek 120 kHz). The third reactor (not shown) is a horizontal low-pressure hot-wall tool, similar in design to reactor A but with a pulsed aerosol injection system that uses a commercial automotive fuel-injector (Ford 2M2EA7B).

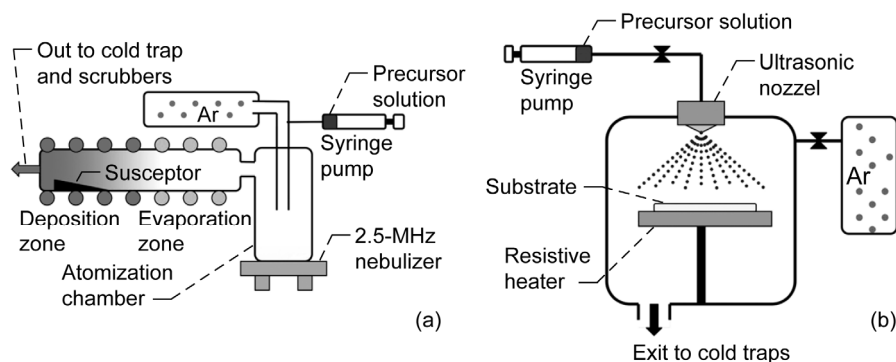


Figure 12.—Two reactors used in AACVD studies. (a) Atmospheric-pressure horizontal hot-wall reactor (reactor A). (b) Vertical cold-wall reactor (reactor B).

Even though all three reactors share the same precursor delivery system, each tool offers specific advantages. For example, a cold-wall reactor (reactor B) helps prevent decomposition of the precursor before it reaches the substrate. A pulsed aerosol injection system at low pressure (reactor C) allows the film to grow under better defined conditions than in a continuous process (reactor A) because of the minimization of undesirable transient effects due to the high volatility of the solvents used (ref. 48). A more detailed description of each of the conditions for film growth, including reactor type, precursor type, delivery method, deposition temperature, growth time, and other parameters are summarized in table II. Depositions were done on bare and Mo-coated glass slides from Corning (Corning 7059 and 2947, respectively). Comm-

ercial Mo foil substrates were also used. Postdeposition annealing of film III was performed in a Lindberg 54477 tube furnace (SPX Corporation) at 600 °C for 10 min under N₂ flow (4 SLPM).

Preliminary Thin-Film Deposition Studies

Our initial efforts involved a cross section of representative precursors for several different solid-state materials on a variety of substrates. The rationale was to demonstrate the utility of this process for producing thin films and devices. Follow-on studies (see below) were intended to further process the most promising candidate films into optimized solar cells.

TABLE II.—GROWTH PARAMETERS FOR AACVD-DEPOSITED CuInS₂ FILMS

Parameter	Film				
	I	II	III	IV	V
Reactor	A	B		C	
Precursor ^a	Solid	Liquid			
Concentration, M	0.01				
Precursor delivery method	Carrier gas			Vacuum-driven	
Delivery rate, ml/min	~1.7	1.5		0.4	
Temperatures, °C					
Evaporation zone	128	120	no zones	250	150
Deposition zone	390	360	400	250	250
Substrate	^b 390	^b 360		420	400
Pressure, torr	760 (atmospheric)			~12	~10
Ar flow rate, liter/min	4			^c 0.08	^c 0.15
Substrate ^d	Mo/glass	Mo foil	Glass	Mo/glass	
Substrate dimensions, cm	0.87×7.6×0.1		2.5×2.5×0.1	2.5×7.6×0.1	
Growth time, min	80		60	250	
Film thickness, μm	~1		~4	~1	

^aSolid precursor is [{PPh₃ }₂Cu(SEt)₂In(SEt)₂], **1**, and liquid precursor is [{PBuⁿ }₃]₂Cu(SEt)₂In(SEt)₂], **7**.

^bSubstrate is located within the deposition zone.

^cDirect reading from MKS flow controller (not calibrated). Ar flow is required for the aerosol creation mechanism.

^dMo-coated glass slides were Corning 2947, and bare glass slides were Corning 7059, from Corning, Inc.

CuInS₂ growth on molybdenum

Well-adhering dark blue-black CuInS₂ films were deposited on a molybdenum substrate by spray CVD at 390 °C using [PBU₃]₂Cu(SEt)₂In(SEt)₂ (SSP 7 in table I). As deposited, the CuInS₂ films were preferentially (112) oriented (fig. 13); this is significant for producing solar cells, since (112)-oriented films tend to have a low series resistance (ref. 49).

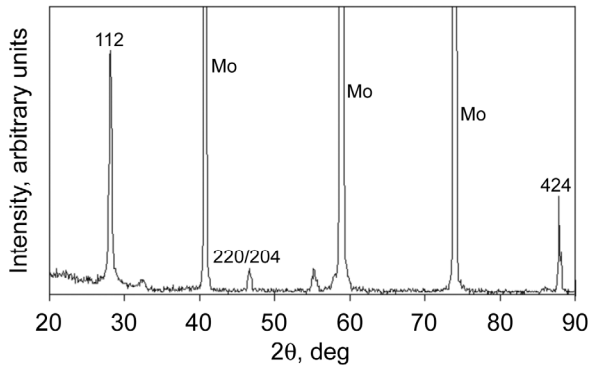


Figure 13.—Powder x-ray diffraction (XRD) spectrum of CuInS₂ thin film on Mo, grown from [PBU₃]₂Cu(SEt)₂In(SEt)₂ (precursor 7 in table I).

Measurements of the EDS emission were limited to Cu and In edges since the EDS emissions for sulfur and molybdenum overlapped. SEM-EDS data on a number of regions on the film gave atomic percents representative of CuInS₂ (table III), and no evidence of phosphorous could be detected under the typical detection limit of EDS (0.02 wt%), verifying that the precursor decomposes cleanly as evidenced in EGA-TGA studies.

TABLE III.—ATOMIC COMPOSITION OF CuInS₂ THIN FILM DEPOSITED USING SSP [PBU₃]₂Cu(SEt)₂In(SEt)₂, 7

Element	Atomic percent (±3%)		
	Front 1	Front 2	Back
Cu	50	51	50
In	50	49	50

Schottky diode growth

The electrical properties of the films deposited using SSP 1 (fig. 14) were evaluated by current versus voltage (*I*-*V*) measurements recorded for the thin films using thermally evaporated aluminum contacts (10 mm²), to make Schottky barrier diodes (see fig. 15).

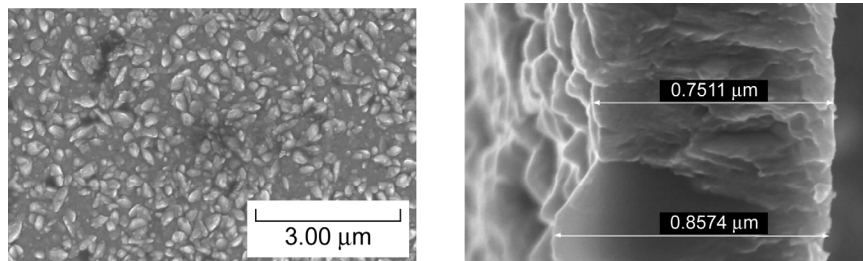


Figure 14.—Scanning electron micrographs of deposited CIS film grown from [P(PPh)₃]₂Cu(SEt)₂In(SEt)₂ (precursor 1 in table I). (a) Plane view. (b) Cross-sectional view.

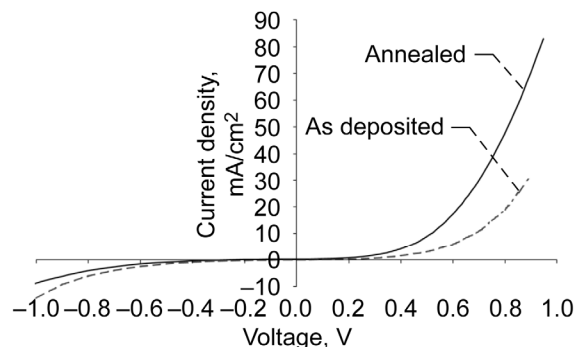


Figure 15.—Current density versus voltage plot of Schottky barrier made from evaporated Al on CuInS₂ on Mo foil grown from [PPh₃]₂Cu(SEt)₂In(SEt)₂ (precursor 1 in table I).

The Schottky barriers were excellent diodes on films annealed at 600 °C, with “turn on” voltages of 0.6 to 0.8 V and minimal reverse bias leakage (ref. 50). However, many of the contacts on the as-deposited films gave large reverse bias currents and nearly ohmic responses. This behavior is indicative of degeneracy of the semiconductor due to a high carrier density resulting from native defects. The improvement in the diode behavior of the annealed films is attributed to enhanced crystallinity and reduction of defects.

Growth and characterization of CuGaS₂ films

Spray CVD deposition studies with a new Ga SSP **9**, in a toluene-CH₂Br₂ solution (86 vol% toluene) afforded well-adhered dense films, (450±5 °C, 4.0 SLPM). The films were visually smooth and optically transparent, exhibiting a pink and green surface tint. XRD analysis confirmed the film to be highly (112)-oriented, tetragonal, single-phase CuGaS₂ (see fig. 16).

The (220)/(204) reflections and the (312)/(116) reflections were split (fig. 16) consistent with the tetragonal distortion of the crystal lattice (ref. 51). Lattice parameters *a* and *c* were calculated from X-ray *d*-spacings according to equation (5):

$$\frac{1}{d^2} = \frac{h^2 + k^2}{a^2} + \frac{l^2}{c^2} \quad (5)$$

where *h*, *k*, and *l* refer to the Miller indices of individual reflections (ref. 52). The *d*-spacing of the (220) reflection was used to calculate *a* and the *d*-spacing of the (112) reflection

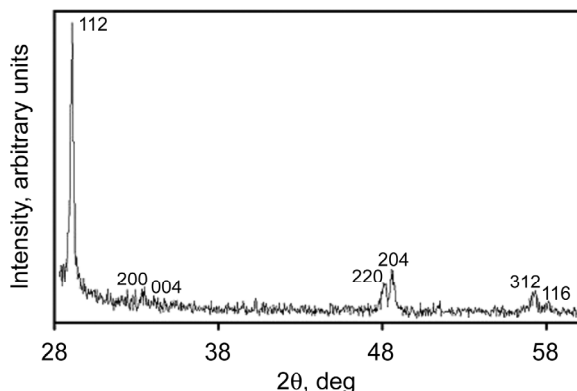


Figure 16.—X-ray diffraction pattern of spray-CVD CuGaS₂ film on Si(111) grown from [PPh₃]₂CuGa(SEt)_x (precursor **9** in table I). Reflections correspond to those reported for CuGaS₂ in Powder Diffraction File 00–25–0279, ref. 44).

was used, with the calculated lattice parameter *a*, to determine *c*. The lattice parameters, *c/a* ratio, and the distortion parameter *x* (where $x = 2 - c/a$, given that a hypothetical *c/a* ratio of 2 would result in the absence of any tetragonal distortion) are presented in table IV. Comparison of the data collected from the CuGaS₂ film shows they are in good agreement with the JCPDS reference values for single-crystal CuGaS₂ and with those reported in the literature (ref. 53).

TABLE IV.—COMPARISON OF THIN FILM AND SINGLE-CRYSTAL CuGaS₂ LATTICE PARAMETERS (*a* AND *c*), *c/a*, AND DISTORTION PARAMETER *x*

CuGaS ₂ sample	<i>a</i> , Å	<i>c</i> , Å	<i>c/a</i>	<i>x</i>
Spray CVD film	5.353	10.495	1.9606	0.0394
Evaporated film (ref. 52)	5.35	10.48	1.959	0.0410
Single crystal prepared from elements ^a	5.351	10.484	1.9593	0.0407

^aPowder Diffraction File 00–25–0297, reference 44.

SEM images reveal that the films are dense, with predominantly columnar grains on the surface of the substrate and with an average grain size of 410 nm (see figs. 17(a) and (b)). The surface microstructure consisted of faceted grains, many of which exhibited a trigonal shape (figs. 17(c) and (d)), which occurs as a result of close-packed intersecting (112) faces of the chalcopyrite lattice. These are the lowest surface-energy faces, and they typically control chalcopyrite morphology (refs. 34 and 54). The grain sizes observed by SEM are considerably larger than the average coherence lengths calculated from x-ray line broadening, which could have been reduced by a high defect density in the grains or by strain in the film.

Sheet resistance (*R_s*) is defined by $\rho = R_s t$, where ρ is resistivity and *t* is film thickness. For CuGaS₂ thin-film samples, *R_s* was determined using the four-point probe method (ref. 55) and calculated from current-voltage data (fig. 18) by equation (6):

$$R_s = K_p \left(\frac{V}{I} \right) \quad (6)$$

where *K_p* is a constant. The linear region below 3.0×10⁻² mA on figure 18 was used to calculate sheet resistance. For a probe of the type used here and for a sample with planar dimensions that can be considered infinite relative to the probe spacing, $K_p = \pi/\ln 2$. The resistivity determined for the film deposited at 450 °C on fused silica was found to be 15.6(4) Ω-cm, which is comparable to values reported in the literature (ref. 55).

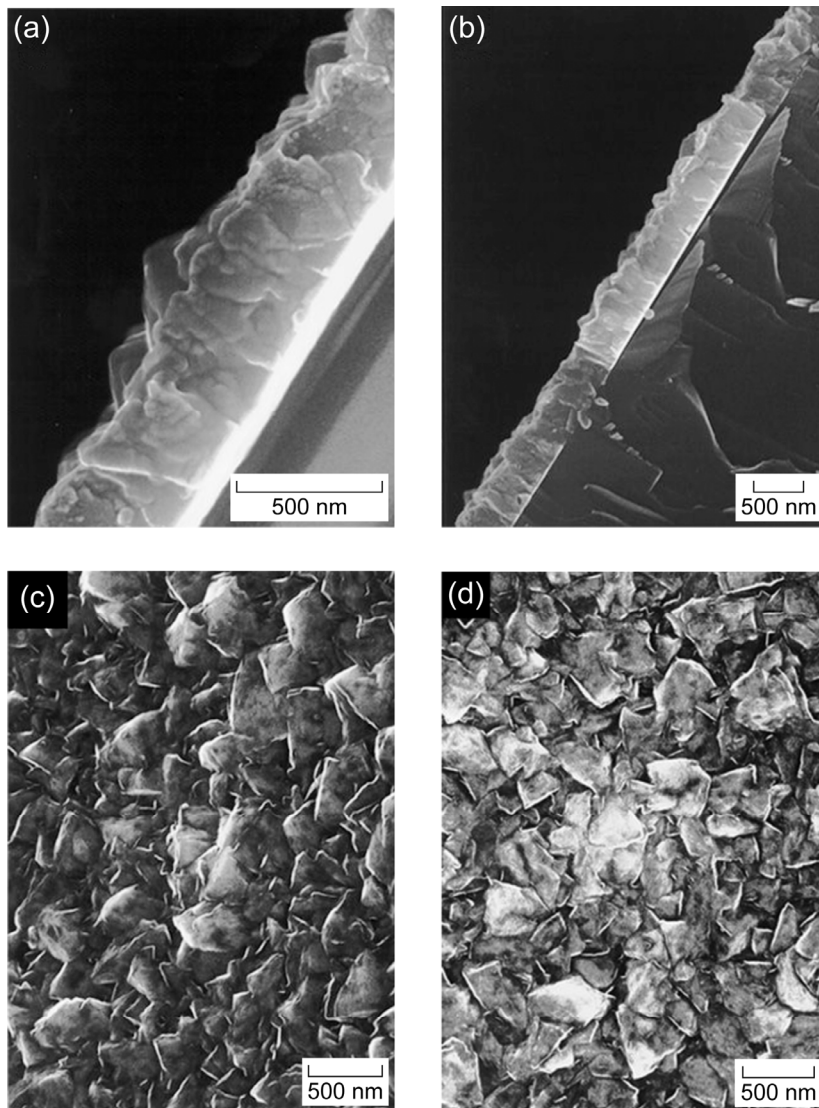


Figure 17.—Scanning electron microscopy images of CuGaS_2 films deposited by AACVD. (a) Expanded edge view showing triangular grains protruding from film surface. (b) Edge view. (c) Surface view of 30° tilt. (d) Surface view.

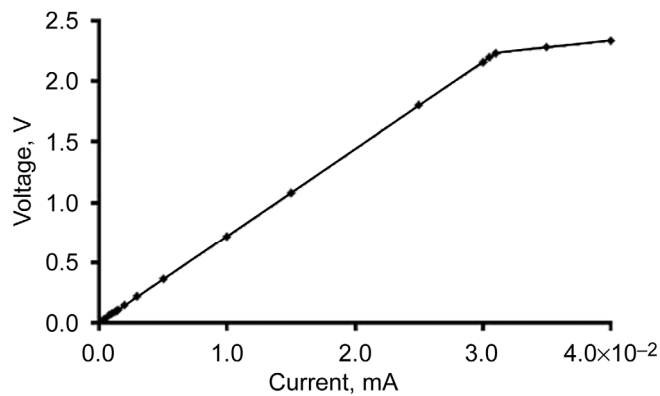


Figure 18.—Current-voltage (I - V) curve for CuGaS_2 thin film grown from $[\{\text{PPh}_3\}_2\text{CuGa}(\text{SEt})_x]$ (precursor **9** in table I).

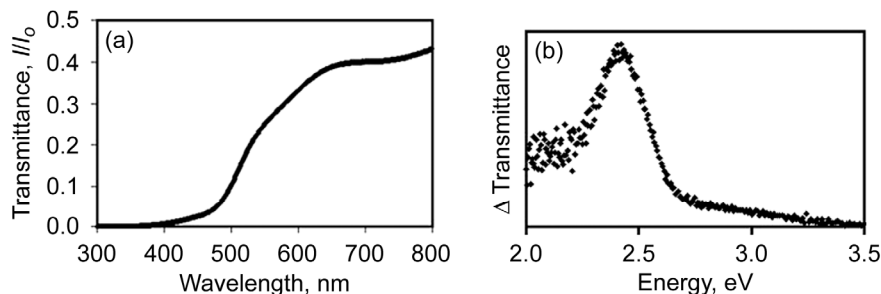


Figure 19.—Optical transmittance data for CuGaS_2 thin film. (a) Transmittance versus wavelength (I = transmitted power, I_0 = incident power). (b) Plot of derivative of transmission data versus energy.

The optical bandgaps of the films were determined from optical transmittance data, which showed the films to absorb incident light below 480 nm (fig. 19(a)). Transmittance was observed to change most dramatically in the region from 480 to 540 nm, which is the region of the direct absorption edge. Calculation of the derivative for the transmission curve provided a more precise method to determine the bandgap within this region (refs. 53 and 57), yielding a maximum at 2.42 eV (fig. 19(b)). This value is in very good accord with the known direct bandgap of CuGaS_2 , $E_g = 2.43$ eV, as reported in the literature (ref. 57).

Dual-source AACVD study

Initial studies using the two analogous Ga and In SSPs for fabrication of an alloy film $\text{Cu}(\text{In}:\text{Ga})\text{S}_2$ in a dual-source spray CVD were also investigated. A film was deposited from a mixed toluene solution of [$\{\text{Ph}_3\text{P}\}_2\text{Cu}(\mu\text{-SEt})_2\text{In}(\text{SEt})_2$] **1** (0.0075 M) and the Ga analog **9** (0.0025 M) (ref. 3). Although a thin film was deposited, composition and microstructure varied along the length of the film, which may be attributed to the “boundary layer” model for velocity, temperature, and reactant concentration for horizontal CVD reactors (ref. 34). XRD reflections representing the (112) planes were broad and complicated by the presence of an unidentified reflection in that region. The (220)/(204) planes were represented by a single unresolved reflection that yielded an average grain size of ~ 40 nm. The relative contribution of Ga and In to the intermediate-composition patterns was determined by comparing the 2θ values for this reflection in the multinary pattern with those in the patterns of the ternary end-members, CuInS_2 and CuGaS_2 (fig. 20). The composition of each metal was assumed to vary linearly with 2θ from 100 percent In to 100 percent Ga based on Vegard’s Law. The tetragonal splitting was neglected in the CuGaS_2 pattern by averaging the 2θ values for the 220 and the 204 reflections.

The atomic percent of Ga in the film was found to increase along the substrate from the front to rear of the film. The film deposited in the first centimeter had a composition of $\text{CuIn}_{0.43}\text{Ga}_{0.57}\text{S}_2$. In the middle portion of the film the composition was $\text{CuIn}_{0.38}\text{Ga}_{0.62}\text{S}_2$ (statistically indistinguishable from the first centimeter), while the last

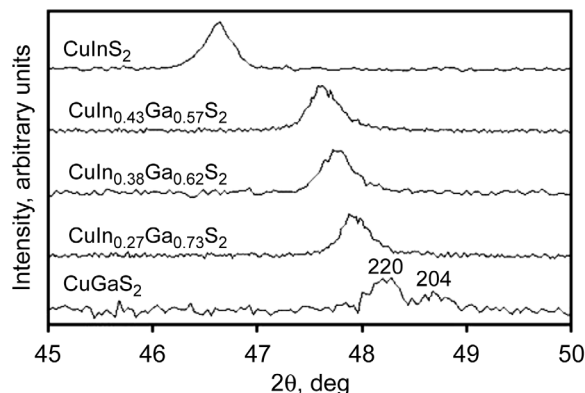


Figure 20.—X-ray diffraction (XRD) spectra highlighting the 220/204 reflections of a CuGaS_2 film (bottom; $T_s = 450$ °C), a CuInS_2 film (top; $T_s = 450$ °C) and alloy films having variable In_xGa_y ratios as noted. All films were deposited on fused silica.

centimeter of the film had the highest contribution of Ga (i.e., $\text{CuIn}_{0.27}\text{Ga}_{0.73}\text{S}_2$). A uniform composition over large areas was therefore not achieved and, interestingly, none of the compositions were close to the expected $\text{In}_{0.75}\text{Ga}_{0.25}$ ratio in accord with the precursor molar ratio. SEM images of the films (fig. 21) revealed that the microstructure was similar to that observed for CuInS_2 deposited at 450 °C (ref. 41). The variation in film composition is understandable since the thermal decomposition profiles of the two precursors are unlike. Therefore, using two SSPs with matching thermal profiles might provide a more effective means for depositing quaternary films.

Impact of Reactor Design on CuInS_2 Film Growth

In a follow-on precursor decomposition study, three different reactors were used to grow CuInS_2 films (see table II). Hot-wall reactors A (film I) and C (films IV and V) produced dense, columnar grain growth, while the cold-wall reactor B (film III) yielded porous nanostructures (see SEM micrographs in fig. 22, and see table II for deposition conditions). The thickness of the films produced from each

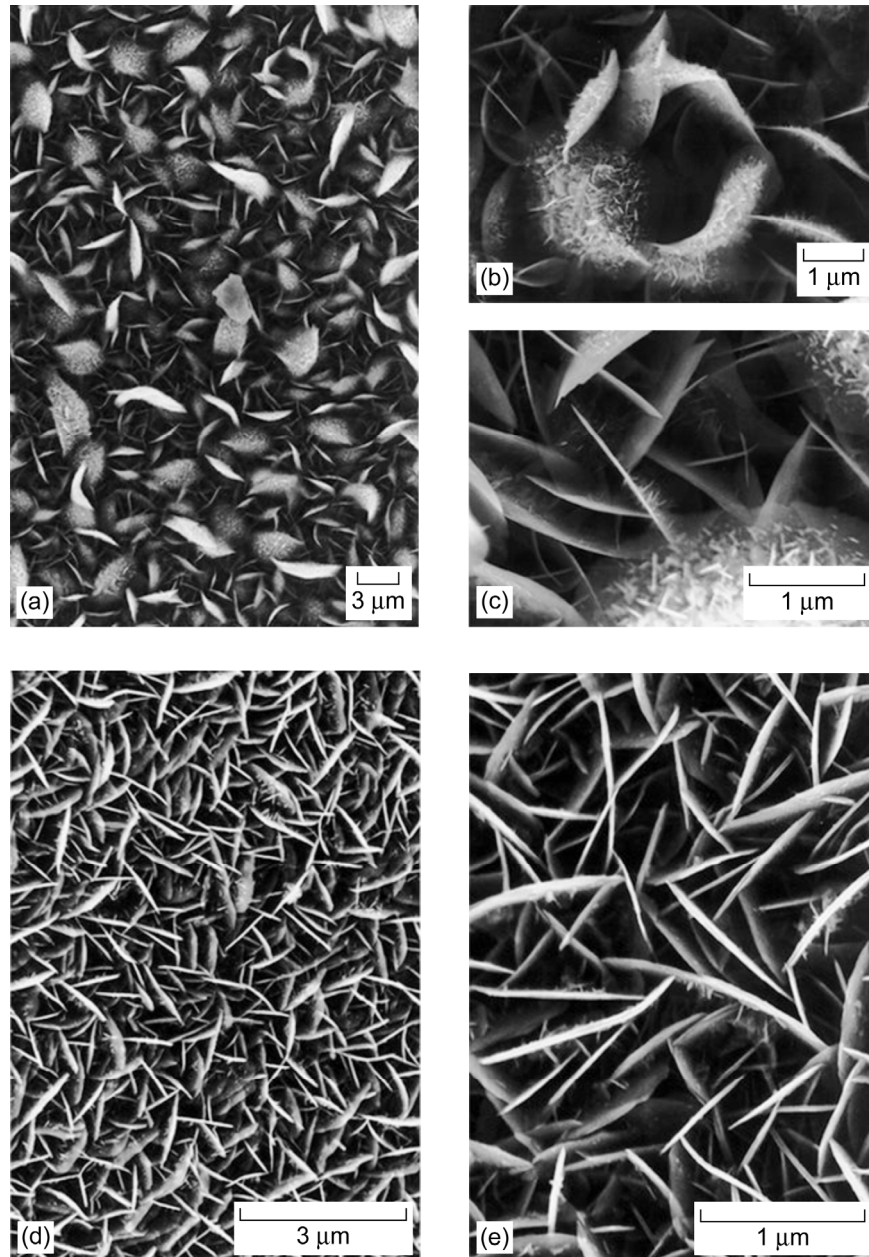


Figure 21.—Scanning electron micrographs (SEM) of the alloy $\text{Cu}(\text{In:Ga})\text{S}_2$ film showing the variation in microstructures with composition. $\text{CuIn}_{0.43}\text{Ga}_{0.57}\text{S}_2$ films were deposited in first centimeter, and $\text{CuIn}_{0.27}\text{Ga}_{0.73}\text{S}_2$ films were deposited in last. (a) $\text{CuIn}_{0.43}\text{Ga}_{0.57}\text{S}_2$, lowest magnification. (b) $\text{CuIn}_{0.43}\text{Ga}_{0.57}\text{S}_2$, higher magnification. (c) $\text{CuIn}_{0.43}\text{Ga}_{0.57}\text{S}_2$, highest magnification. (d) $\text{CuIn}_{0.27}\text{Ga}_{0.73}\text{S}_2$, lower magnification. (e) $\text{CuIn}_{0.27}\text{Ga}_{0.73}\text{S}_2$, higher magnification.

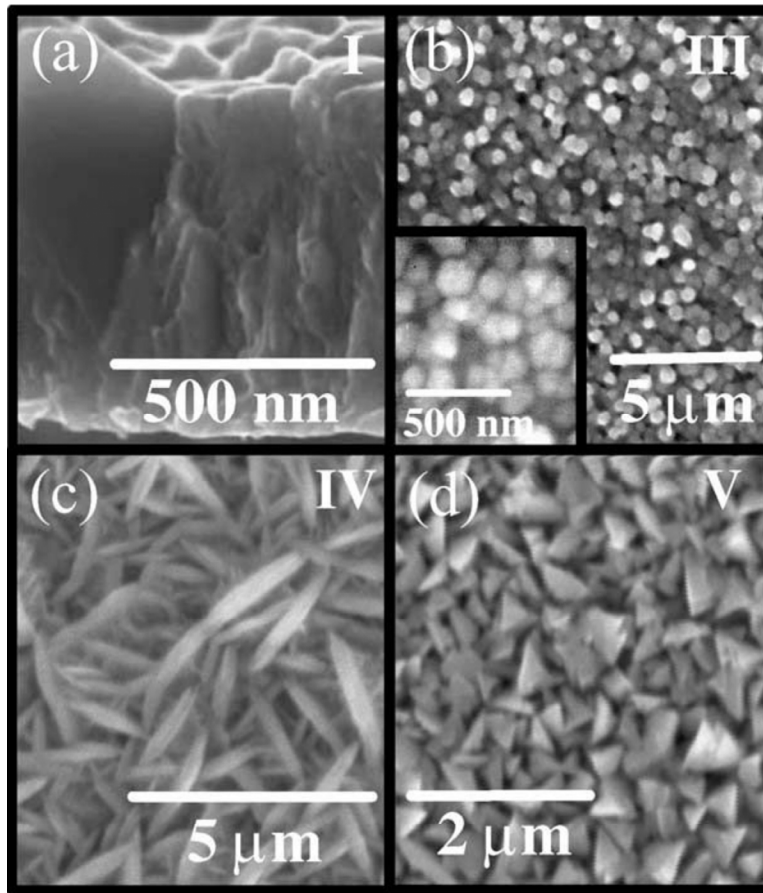


Figure 22.—Scanning electron micrographs (SEM) of AACVD-grown CuInS_2 thin films (see table II for growth parameters). (a) Cross-sectional view of film I. (b) Plane view of film III (inset at higher magnification). (c) Plane view of film IV. (d) Plane view of film V.

reactor were similar in magnitude, thus supporting the notion that film thickness is directly proportional to solution molarity. Film roughness was found to vary between reactors, but further studies are needed to determine if reactor design was responsible or if thin-film fabrication process parameters were not optimized. Figure 22(a), the cross-sectional image of film I, shows a columnar grain structure. The columnar grain structure lowers the cross section for photo-excited carrier recombination at grain boundaries, thus improving the performance of the solar cells.

Figure 22(b) shows a plane-view image of film III together with an inset of the same region at a higher magnification. Under low magnification, only the round structures appeared. However, when the magnification was increased, smaller nanoparticles (~ 100 nm) were seen. The nanoparticles may have been created above the hot substrate by pyrolysis of nanodroplets generated from the aerosol (ref. 58). Under this model, the ultrasonically excited aerosol continues to flow through until it breaks into numerous nanodroplets. Other proposed models include nanoparticles coagulating before landing on the growth surface (ref. 59) and liquid deposition

taking place instead of vapor deposition because of the partial evaporation of the liquid droplet (ref. 60).

Film IV can be seen in figure 22(c) exhibiting a dendritic microstructure with nonfaceted, elongated grains. It was previously proven that this was a consequence of diffusion-limited growth (ref. 40). By increasing the flow rate, dense and trigonal-shaped faceted grains were obtained for film V (fig. 22(d)). This shape is due to the intersection of $\{211\}$ faces in the chalcopyrite structure. The largest grain sizes obtained in this study using SSPs were for film V, of the order of $0.5 \mu\text{m}$.

The XRD patterns revealed that the films were either (112) or (220)/(204) oriented. Differentiation between the chalcopyrite and sphalerite phases was made by differences in XRD patterns (ref. 61). The XRD patterns for all five films can be seen in figure 23(a). It was found that films often contained a secondary phase ($2\theta = 26.5^\circ$), believed to be indium-rich (In-rich) (ref. 7). The more In-rich the film, the more likely it was that the secondary phase was present, with the film being more (220)/(204) oriented. EDS measurements

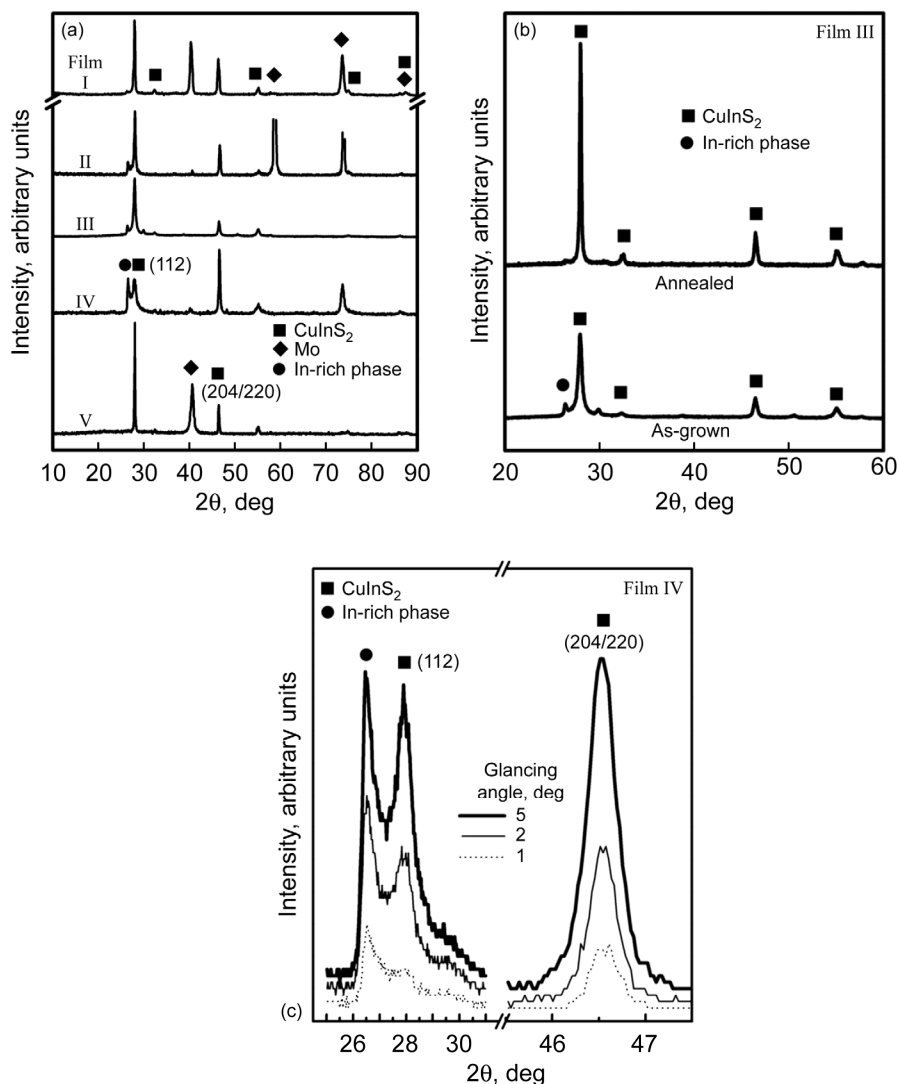


Figure 23.—X-ray diffraction (XRD) spectra of CuInS_2 films grown by AACVD (see table II for growth parameters). (a) Untreated films. (b) Film III with post deposition annealing. (c) Glancing angle XRD spectrum of film IV.

(not shown) indicate that the films containing the secondary phase were In-rich and that the Cu/In ratio increased when the secondary phase was reduced upon annealing (fig. 23(b)). In order to confirm the In-rich nature of the secondary phase, GAXRD was performed on the films. The GAXRD pattern (fig. 23(c)) revealed that the secondary phase was concentrated at the surface. In order to find out the chemical nature of the phase, films containing the phase were etched in a 10 percent aqueous KCN solution for 2 min. It is common to etch Cu-rich CuInS_2 films in this solution prior to CdS deposition to remove undesired CuS_x compounds segregated on the surface during CuInS_2 deposition. In addition, it is also known that the etch rate of Cu-rich compounds in KCN solutions is much higher than for In-rich compounds (ref. 62). After etching, GAXRD still showed the presence of the secondary phase on the surface without any change in its

diffraction intensity, meaning that the phase is not CuS_x . The nature of the secondary In-rich phase was also confirmed by Raman spectroscopy (ref. 7).

Processing conditions were sought to prevent the formation of the secondary phase, to favor growth conditions of (112)-oriented films, and to avoid the surface kinetic regime where a (220)/(204)-oriented film is favored. In our setup, for any reactor, the substrate temperature had to stay around 400°C in order to promote the growth of (112)-oriented films without a high concentration of the In-rich secondary phase. Another way to decrease the amount of this secondary phase is by postdeposition heat treatment.

Bandgap energies between 1.45 and 1.47 eV were obtained for the films. The bandgap energies were estimated using plots of $(\alpha h\nu)^2$ versus E (fig. 24), where α is an absorption coefficient estimated from optical transmittance data and $h\nu$ is

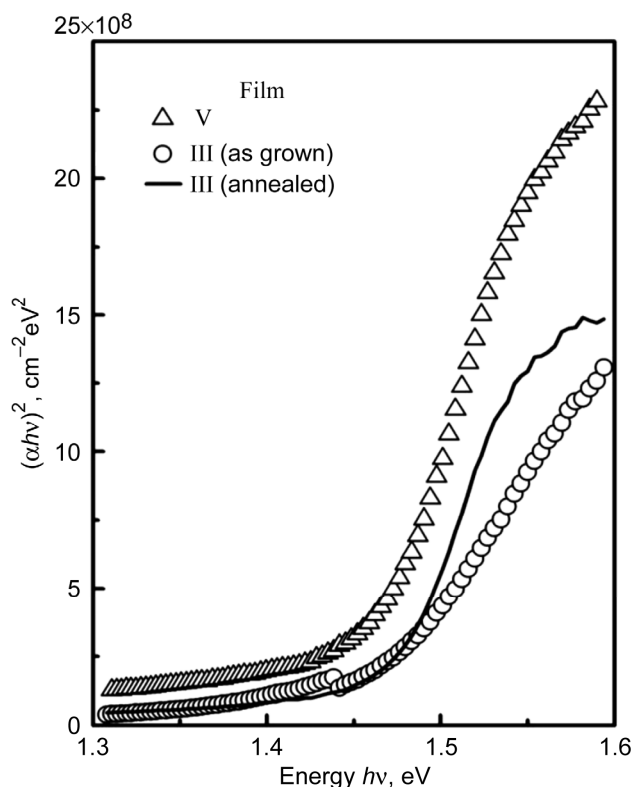


Figure 24.—Plot of $(\alpha h\nu)^2$ versus energy $h\nu$ for CuInS_2 films III and V, where α is the extinction coefficient. See table II for growth parameters.

the photon energy, E . Figure 24 shows that the band edge sharpens upon postgrowth annealing, which is ascribed to improved crystallinity and densification (film III). The overall absorption of film V was higher than that of film III in the figure, and this could be attributed to the difference in the density between the two films: film V had a denser grain structure than film III, as shown in figure 22.

All of the films grown showed p-type conduction regardless of the reactor type, Cu/In ratio, or morphology. It has been reported that S-rich material shows p-type conduction (refs. 63 and 64) and that the Cu-on-In antisite (Cu_{In}) in Cu-rich films is expected to be the major acceptor for p-type conduction (ref. 49). The bulk resistivities ranged from 0.1 to 30 $\Omega\cdot\text{cm}$; Cu-rich films generally had lower resistivity than In-rich films.

Atmospheric-Pressure Hot-Wall Reactor Parametric Study

The reactor used for this study was the horizontal atmospheric-pressure hot-wall reactor (reactor A in fig. 12). The susceptor accommodated three substrates side by side at an angle of 15.5° above horizontal. The leading edge of the film experiences a more reactant-rich gas stream and is closer to the bottom of the reactor. The environment of the trailing

edge, deeper in the deposition zone, is more product-rich and is closer to the axial center of the reactor tube.

In order to optimize thin film and device quality, a four-phase study was conducted. The temperature of the deposition zone, location of the susceptor in the deposition zone along the length of the reactor tube, concentration of the precursor solution, and postdeposition annealing conditions were varied individually. Initially, the substrate temperature was varied between 350 and 425 $^\circ\text{C}$. In the second phase, the measured distance from the end of the reactor tube up to the trailing edge of the susceptor was varied from 57.15 to 127 mm (2.25 to 5 in.). The larger the distance, the closer the susceptor (and substrate) is to the warm evaporation zone. For phase three, the precursor concentration was varied between 0.005 and 0.04 mol/liter. The deposition temperatures for the two middle parts of the experiment were maintained at a fixed value of 395 $^\circ\text{C}$. Finally, postdeposition annealing of films was performed in the reactor. The evaporation zone temperature was set to 120 $^\circ\text{C}$, and run-to-run deposition zone temperatures were varied between 450 and 580 $^\circ\text{C}$. During annealing, argon was flowed through the reactor tube at a rate of 10 ml/min. Annealing times varied from 15 min to 17 h. The annealing times began when the annealing temperature was reached and ended when the cooling process started. It took about 30 min to reach the annealing temperature when starting at room temperature and a little over 1 h to cool down to room temperature. For some runs, sulfur vapor was added during annealing by placing powdered sulfur (Strem Chemicals, 99+%) in a crucible in the evaporation zone.

As discussed above, in this study various reactor parameters were manipulated in order to observe their effects on film growth. In general, the leading edge of the films tended to be smooth, shiny, and dense, while the trailing edge tended to be rough, dull, and highly porous. The rough surface morphology can be attributed to the stronger diffusion-limited film growth at the trailing edge (ref. 65). By the time the carrier gas (Ar) reaches the trailing edge of the substrate, it is likely to be less precursor-rich than the gas flowing over the leading edge: Reaction occurs on the hot wall of the reactor along the deposition zone. This would make the concentration boundary layer thicker at the trailing edge of the substrate, requiring the precursor to diffuse a greater distance to reach the surface of the trailing edge and hence the film growth would be more diffusion limited. The SEM images of a smooth, shiny film can be seen below in figure 25(a); the images of a rough, dull film can be seen in figure 25(b).

Variation of Deposition Temperature

Deposition zone temperature from run to run (350 to 425 $^\circ\text{C}$) was the first parameter varied. Temperature variation affected film stoichiometry (fig. 26(a)) and crystalline orientation (fig. 26(b)), while not significantly affecting the deposition rate (fig. 26(c)). From figure 26(a), the films are seen to be closest to stoichiometry when deposited at 395 $^\circ\text{C}$. Cu-to-In ratios ranged from 0.79 to 0.98, with the highest ratio

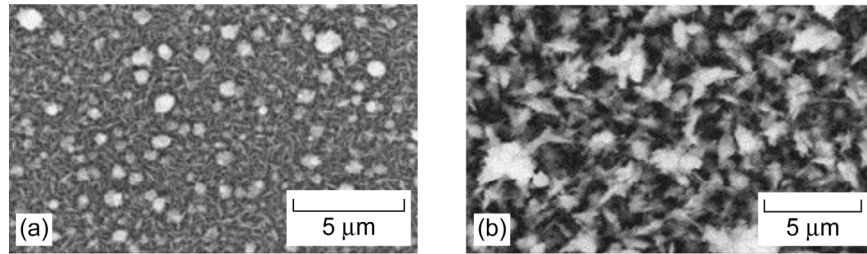


Figure 25.—Scanning electron micrographs (SEM) of CuInS_2 films grown by AACVD. (a) Smooth, shiny, dense film on leading edge. (b) Porous, rough, dull film on trailing edge.

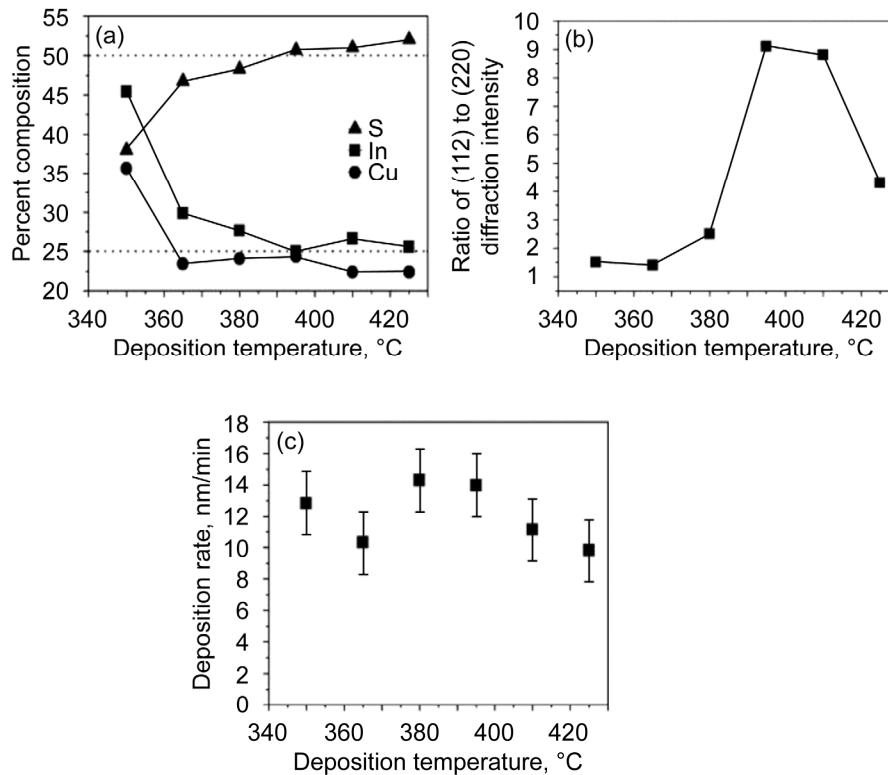


Figure 26.—Affect of deposition temperature on AACVD of CuInS_2 films with precursor feed rate of 1.6 g/h. (a) Elemental composition of films. (b) Crystalline orientation of films. (c) Deposition rate of films.

occurring also at 395 °C. The higher deposition zone temperature correlated to increased sulfur content in the films. The increased surface mobility at higher temperatures would favor increased inclusion of sulfur.

CuInS_2 films deposited in this study were observed to be crystallographically (220)/(204) oriented or (112) oriented by XRD. Chalcopyrite solar cells had a higher series resistance for the (220)/(204)-oriented films (ref. 66). From XRD measurements in figure 26(b), deposition temperatures of around 395 °C were observed to yield higher ratios of the preferred (112)-oriented films. Finally, deposition rates were not limited by supply of thermal energy (temperature variation). Therefore film growth was not reaction limited, as seen in figure 26(c).

Variation of Susceptor Location and Precursor Concentration

The next parameter varied was the location of the susceptor within the deposition zone. Variations of the susceptor location did not affect film stoichiometry, but they did influence the morphologies of the films. When the susceptor was moved towards the evaporation zone, denser-, smoother-, and shinier-looking films were obtained because of a reduced concentration boundary layer (less diffusion limited) towards the evaporation zone.

The single-source precursor concentration in the carrier solvent was another parameter that was varied. The concentrations of the SSP in toluene were varied between

0.005 and 0.04 mol/liter. There were no significant changes in elemental composition of the films as a function of concentration, but increasing the precursor concentrations gave smoother, shinier films than with lower concentrations. This is because at higher precursor concentrations, more precursor compound was available to the film reaction surface, reducing the effects of a diffusion-limited growth process.

Postdeposition Annealing

The final parameter manipulated was postdeposition annealing. It was determined that postdeposition annealing improves the elemental composition and crystalline structure of films. For example, after a 5-h anneal at 580 °C in a sulfur-rich atmosphere, typical film elemental compositions (at.%) changed from 51.5 %S, 24.5 %In, and 24.0 %Cu to 52.0 %S, 23.5 %In, and 24.5 %Cu, measured by EDS. Although the compositional change in bulk is minimal, annealing might improve the electronic properties of films by removing the volatile residual In-rich secondary phase and surface states that are detrimental to the performance of solar cells. For example, it is reported that increasing the Cu/In ratio improved electrical properties of CuInS₂ films (ref. 67) and that annealing in a sulfur-rich atmosphere passivates sulfur vacancies, an undesirable n-type dopant (ref. 68). Ordering of the Cu and In atoms within the crystalline structure also increased, producing a better ordered chalcopyrite film.

Evidence of a more ordered chalcopyrite structure can be seen in figure 27, where the (101) and (211) diffractions at 17.9° and 37.3°, respectively, can be clearly seen in the annealed film. Another characteristic of the chalcopyrite structure not seen in the sphalerite structure is the peak splitting in the (200)/(004) and (116)/(312) diffractions at 32.2°/32.4° and 54.8°/55.1°, respectively (fig. 27, inset). The highest power conversion efficiency for a cell made with an AACVD-deposited film using SSPs was 1.0 percent and the film was annealed under sulfur and argon at 450 °C for about 7 h (ref. 8). The highest efficiency for a cell made with a nonannealed film was 0.9 percent (ref. 8). Both cells had smooth, shiny, and dense CuInS₂ absorber layers.

Photoluminescence Studies

Films annealed at 450 °C for 7 h were characterized using photoluminescence (PL). It has been previously shown that annealing can remove structural defects associated with metal ions in films, thereby improving the electronic properties of the absorber layer (refs. 69 and 70). CuInS₂ films were excited using an Ar ion laser system (Coherent Innova 70) with an excitation wavelength of 514 nm. In order to control the laser power density, neutral density filters were used. The PL emission detection system consisted of a Symphony liquid-nitrogen-cooled charge-coupled device (CCD) (HORIBA Jobin Yvon), a germanium detector (EG&G Judson, J16D) and a lock-in system (Stanford Research Systems,

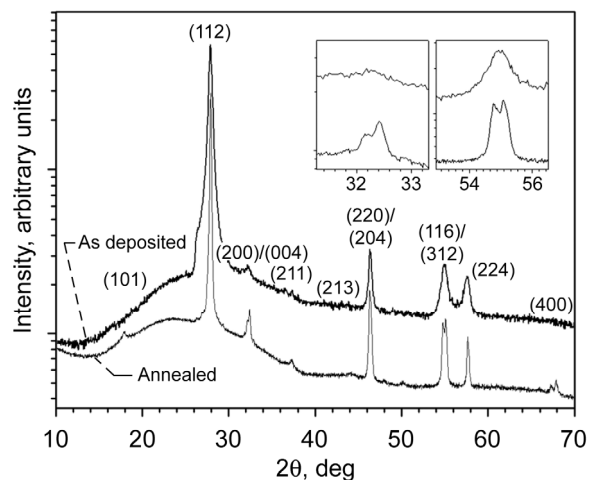


Figure 27.—X-ray diffraction spectra of as-deposited CuInS₂ film and CuInS₂ film annealed at 450 °C for 7 h. Inset shows expanded scale emphasizing peak splitting.

SR810 DSP). The detectors were connected to a Spex 1269 monochromator (HORIBA Jobin Yvon), while the samples were mounted on a helium cryostat (Janis, STVP-100) in order to lower the temperature to 4 K. Finally, devices were tested using a solar simulator at Glenn (Boeing Spectrolab X-25 Mark II) to obtain current versus voltage curves under AM0 illumination (see fig. 2). Calibration was performed using a standard GaAs single-junction solar cell.

Photoluminescence measurements were performed on 76-mm- (3-in.-) long annealed films grown by the process used in the above (parametric) study. Photoluminescence spectra of the leading and trailing edges were recorded for as-deposited, sulfur-annealed, and argon-annealed films. As mentioned in previous sections, the leading edges were always more In-rich than the trailing edges and therefore had lower Cu-to-In ratios (0.84 compared with 1.03). Four different emission bands—PL1 at 1.45 eV, PL2 at 1.43 eV, PL3 at 1.37 eV, and PL4 at 1.32 eV in figure 28—were identified in both the leading and trailing edges of almost all samples (PL1 was not clearly seen in some samples). For the as-deposited films, a near-band-edge emission can be seen for the trailing edge sample in figure 28. This is probably due to the combination of excitonic recombination and other transitions associated with unidentified shallow defect levels (ref. 70). Clear differences between the leading and trailing edges were observed from emission bands associated with deeper defect levels. For the trailing edges, the intensities of PL3 at 1.37 eV were always higher than those of PL4 at 1.32 eV (fig. 28). Finally, the broad, deep-level emission bands spanning from 1.32 to 1.24 eV actually tailed down to 0.9 eV, as measured by a Ge detector.

After postdeposition argon and argon-sulfur annealing, the films were studied again using PL. Sulfur anneals reduced the relative intensities of the PL1, PL4, and broad emission bands,

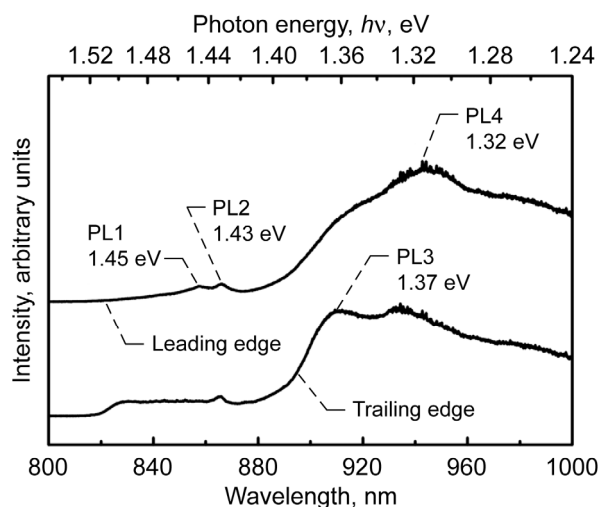


Figure 28.—Photoluminescence (PL) spectra of as-deposited CuInS_2 thin films made from $\{[\text{PPH}_3]_2\text{Cu}(\text{SEt})_2\text{In}(\text{SEt})_2\}$ (precursor 1 in table I).

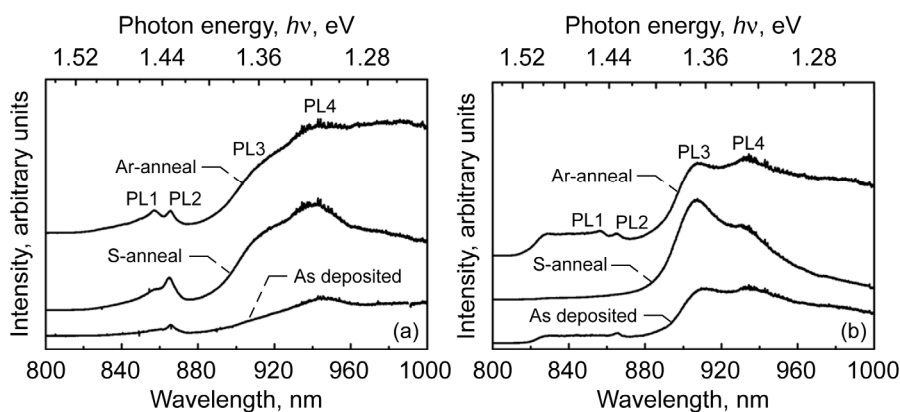


Figure 29.—Photoluminescence spectra of CuInS_2 films prior to annealing and after annealing in either S/Ar or Ar flow at 450°C for 7 h. (a) Leading edge. (b) Trailing edge.

while argon anneals increased the relative intensity of the PL1 band. This can be seen in figure 29. It is also seen in this figure that sulfur anneals suppressed the broad near-band-edge emission from the trailing edge samples. When EDS measurements were performed on the films after sulfur annealing, an extra 1 to 2 at.%S was found incorporated into the films. On the other hand, when argon annealing was performed, 5 to 6 at.%S loss occurred. XRD measurements yielded similar results as above, where more ordered chalcopyrite structures were obtained after sulfur anneals (ref. 8). The sulfur anneals yielded higher resistivity films, while argon anneals yielded lower resistivity films. Hot-probe measurements demonstrated that all annealed films showed p-type conduction.

The excitation intensity was also varied in order to determine the effect it had on the PL spectrum. The PL1 and PL3 bands had a blueshift per decade of 3.7 and 5.5 meV,

respectively, with an increase in excitation intensity. The blueshifts were attributed to donor-acceptor pair recombination (refs. 70 and 71). The PL2 band did not show any excitation power dependency, and the analysis of the PL4 band was not attempted because of the uncertainty in its precise location. The effect of increasing excitation intensity can be clearly seen in figure 30.

The blueshift of the bands with increasing excitation intensity is explained as follows. The emission energy for the recombination can be given by

$$h\nu(r) = E_g - (E_A + E_D) + \frac{e^2}{\epsilon r_{DA}} \quad (7)$$

where E_g is the bandgap, E_A (E_D) is the activation energy of the acceptor (donor), and $e^2/\epsilon r_{DA}$ is the Coulomb energy for

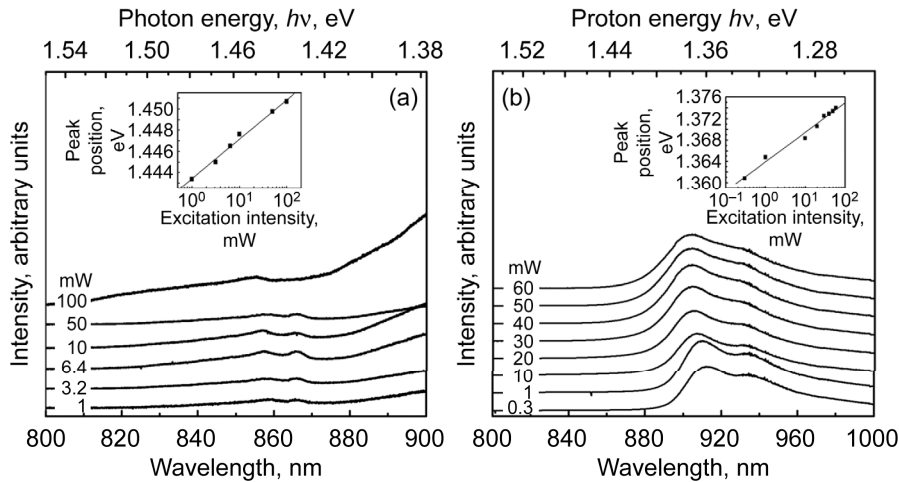


Figure 30.—Spectra of CuInS₂ films with various excitation intensities; inset shows blueshift of emission bands. (a) PL1. (b) PL3.

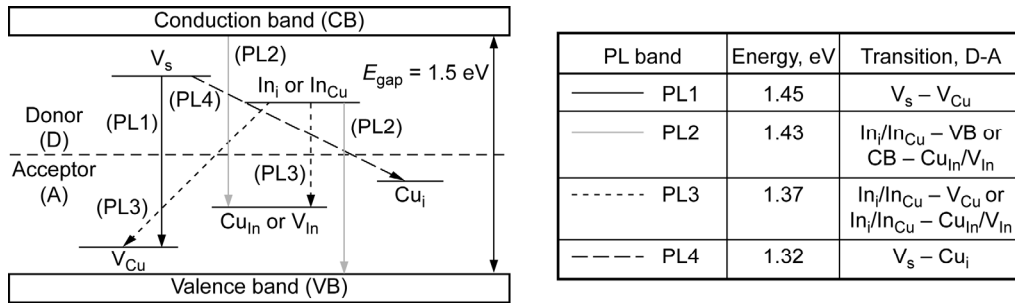


Figure 31.—Scheme 2: Diagram and table of tentative assignment of transitions for the different photoluminescence (PL) bands. Diagram is not drawn to scale.

the pair at a distance r_{DA} (ref. 70). When the excitation energy increases, the film is flooded with photogenerated carriers. As a result, the average separation between the donor and acceptor decreases, causing the blueshift.

Shallow donors and acceptors for CuInS₂ have been previously studied and identified (refs. 68 and 72 to 76). Scheme 2 (fig. 31) includes some of the most energetically favorable intrinsic defects used in this analysis to assign transitions to the four different emission bands. Shallow donors include sulfur vacancy (V_s), In-on-Cu antisite (In_{Cu}), and indium interstitial (In_i). Acceptors include: copper vacancy (V_{Cu}), indium vacancy (V_{In}), Cu-on-In antisite (Cu_{In}) and copper interstitial (Cu_i). The PL1 emission band at 1.45 eV was assigned to a donor-acceptor transition, because of its blueshift upon increasing excitation intensity. V_s was attributed to the donor state because of the band's sensitivity to the change of V_s concentration upon annealing, and V_{Cu} was attributed to the acceptor state because the PL1 intensity was relatively stronger in leading edge (In-rich) samples. The PL2 band at 1.43 eV was assigned to a defect-band transition because there was no noticeable blueshift with increasing excitation intensity. The PL3 band at 1.37 eV was assigned to transitions between metal ions (refs. 68 and 77). Finally, the PL4 band at 1.32 eV was assigned to a V_s - Cu_i transition.

When the film was sulfur annealed, this band was suppressed; sulfur incorporates into the structure, reducing the V_s concentration (ref. 77).

Fabrication and Testing of CuInS₂ Solar Cells

In order to develop an optimal, reproducible approach to fabricating solar cells, absorber layers deposited at NASA Glenn and the University of Delaware Institute for Energy Conversion (IEC) were cross-processed to finished solar cells. The results for Glenn-deposited absorber layers are described below.

Cell Fabrication at Glenn

Complete CuInS₂ solar cells were fabricated at Glenn using the cell architecture shown in figure 32. After coating the glass substrates with Mo, CuInS₂ films were deposited via AACVD, following procedures optimized for the atmospheric-pressure hot-wall reactor (reactor A). Postdeposition sulfur-argon anneals were performed from 450 to 580 °C for up to 17 h. The films were then etched in a 1.5 M KCN solution for 1 min

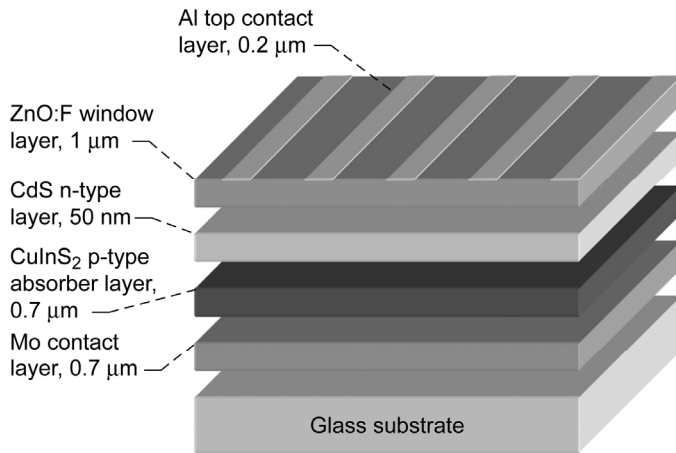


Figure 32.—Schematic of standard NASA Glenn thin-film CuInS_2 solar cell architecture.

at room temperature to remove residual Cu_2S . Cadmium sulfide (CdS) was then deposited on the films using chemical bath deposition (CBD) to form the collecting heterojunction. The CBD used a solution of 0.001 M CdSO_4 , 1.5 M NH_4OH , and 0.0075 M thiourea ($\text{H}_2\text{NC(S)NH}_2$). The bath was heated to 70 °C. Samples were immersed into the bath for 7 to 10 min until the solution started turning yellow. Once the CdS had been deposited, films were placed in an ultrasonic bath to remove particulates. A layer of ZnO:F was deposited from a 16.5-cm- (6.5-in.-) diameter fluorine-doped ZnO target in a radiofrequency sputtering system using pure argon as the sputter gas. Aluminum was used as the top contact metal. A 0.2- μm -thick layer of aluminum was deposited by thermal evaporation through a shadow mask. The devices were isolated by mechanical scribing. The final cell area of the Glenn-produced devices was typically $\sim 0.4 \text{ cm}^2$.

Cross-Fabrication of Solar Cells

Solar cells were also fabricated at the IEC following their well-established fabrication process (ref. 78). This was done in order to isolate issues related to AACVD deposition of CuInS_2 films from those associated with the rest of the solar cell fabrication at Glenn. For the cells prepared at IEC, only CuInS_2 layers were deposited at Glenn. The rest of the device fabrication, including the coating of the glass substrates with Mo and the mechanical scribing, were performed at IEC. Final cell area for IEC-produced devices was typically $\sim 0.45 \text{ cm}^2$. Finally, postfabrication anneals were carried out in air on a hot plate (Cimarec 2) at 150 °C for up to 24 h.

Solar Cell Characterization

The best cell fabricated at Glenn was made from a 0.7- μm -thick CuInS_2 film deposited by AACVD using a 0.01 M solution. After deposition, a sulfur anneal at 450 °C for 17 h was performed. This cell was not annealed after fabrication.

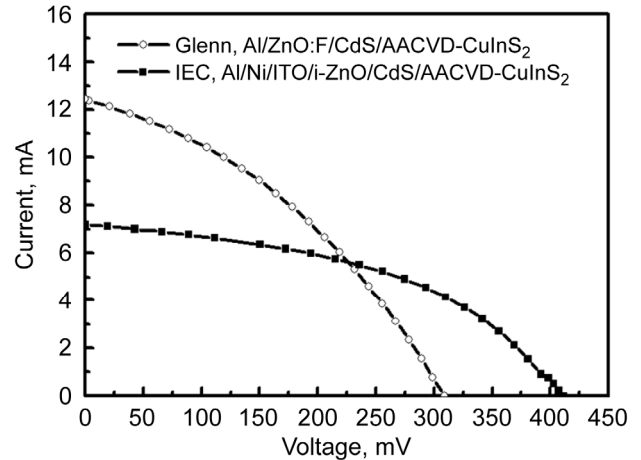


Figure 33.—Light current-voltage characteristics of solar cells fabricated with AACVD-deposited CuInS_2 films from NASA Glenn Research Center and the University of Delaware Institute for Energy Conversion (IEC).

The Mo bottom contact layer had a sheet resistance of 0.5 Ω/sq and a thickness of 0.7 μm . The CdS layer had an optical transmittance of 65 percent at a photon energy of 1.5 eV. Glenn-fabricated cells used a 1- μm -thick, n-type ZnO:F window layer with a sheet resistance of 200 Ω/sq and a transmittance of 85 percent at a photon energy of 1.5 eV. The thickness of the Al top contact was $\sim 200 \text{ nm}$. The current-voltage output characteristic (or performance) curve under light exposure for this cell and cell parameters can be found in figure 33 and table V, respectively. For solar cells, it is common to plot the mirror image of the third quadrant of the conventional current-voltage plot to output characteristics (fig. 33).

Data for the cell fabricated at IEC is also included in figure 33 and table V. This cell was fabricated from a 0.7- μm -thick film deposited using a 0.04 M solution and sulfur annealed at 450 °C for 6 h and 40 min. The completed cell was then annealed under air at 150 °C for about 24 h. This cell's window layer, a 70-nm-thick intrinsic (i-) ZnO layer, had a transmittance of over 90 percent at a photon energy of 1.5 eV. The sheet resistance of the double top contact layer (2 μm Al/50 nm Ni) was about 1.8 Ω/sq . Both cells had nearly the same efficiency (~ 1 percent), but the IEC cell had a higher shunt resistance, which improved the fill factor (see table V). The use of the i-ZnO and the Al/Ni top contact improved the quality of the IEC cells by lowering the series resistance and improving the fill factor, as previously reported in the literature (ref. 18). It should be also noted that most solar cells prepared with the AACVD method in the literature had a superstrate structure (ref. 6). There has been no report of a working device with a typical chalcopyrite solar cell structure (top contact/window layer/CdS/ CuInS_2 /Mo/substrate) except for the authors' previous results (ref. 50).

TABLE V.—AM0^a OUTPUT CHARACTERISTICS OF SOLAR CELLS
FABRICATED WITH AACVD-DEPOSITED CuInS₂ FILMS

Fabricator	Open-circuit voltage, V_{oc} , mV	Short-circuit current, I_{sc} , mA/cm ²	Fill factor	Cell efficiency, η , percent
NASA Glenn Research Center	309	12.5	0.37	1.0
Institute for Energy Conversion	412	7.2	0.45	1.0

^aAM0 is air mass zero (see fig. 6).

Summary of Results

CuInS₂ thin films were grown at low temperatures (<400 °C) via aerosol-assisted chemical vapor deposition (AACVD) using single-source precursors (SSPs) (e.g., (PPh₃)₂Cu(SET)₂In(SET)₂). During the growth process, it was noticed that (112)-oriented films were close to stoichiometric with no secondary phases present, while (220)/(204)-oriented films were In-rich and always included an In-rich secondary phase. This In-rich secondary phase was removed by postprocessing annealing at 600 °C, thereby increasing the Cu/In ratio. The resulting CuInS₂ films always exhibited p-type conduction and bandgap energies of around 1.46±0.02 eV. Films having grain sizes up to 0.5 μm were obtained.

Variation of the deposition zone temperature affected the film stoichiometry and crystalline structure while not significantly affecting the deposition rate. A deposition zone temperature was optimized at 395 °C to produce (112)-oriented films without any detectable secondary phases. The susceptor location within the furnace did not affect the stoichiometry of deposited films, but it did alter morphology. Moving the susceptor towards the evaporation zone improved the morphology of the films. Increasing the precursor concentration in the carrier solvent also increased the density and grain size of the films while not altering the stoichiometry. Energy dispersive spectroscopy and x-ray diffraction analyses indicated that after sulfur annealing the stoichiometry and crystalline structure of the films was enhanced. Photoluminescence studies revealed four major emission bands (1.45 eV, 1.43 eV, 1.37 eV, and 1.32 eV) together with a broad band associated with deep defects. The blueshift of the 1.45 eV and 1.37 eV emission bands with increasing excitation power revealed donor-acceptor pair transitions. The broad band together with the 1.45 eV and 1.32 eV bands were reduced upon sulfur annealing because of passivation of V_s.

These films were then further processed to fabricate working solar cells. The major challenge has been achieving higher open-circuit voltage V_{oc} , which seems to be a problem for cells prepared with AACVD-deposited films in general. It is not yet clear what exactly causes the low V_{oc} and low fill factor of the cells prepared with AACVD deposited films. Further study on remaining issues like defects, junction alignment, recombination losses, and undetected process issues remains to be performed in order to find which material component and/or procedural step is limiting the performance of the solar cells.

Outlook and Future Work

The versatility of the [$\{ER_3\}_2Cu(QR')_2M(QR')_2$] architecture is clearly demonstrated by the preparation of SSPs for multinary semiconductors. Thermal analysis data substantiates that steric and electronic molecular modification on either the neutral donor or chalcogenide permits directed adjustment of the solid-state phase and stability of the precursors. Evolved gas analysis confirms that the decomposition mechanism for the SSPs proceeds “cleanly” by the loss of the chalcogenide moiety, followed by loss of the neutral donor. Spray CVD using SSPs is a mild, simple, clean, and scalable technique for depositing CuInE₂ or CuGaE₂ (E = S, Se) thin films on flexible polymer substrates at reduced temperatures. Although tests for the deposition of the wide-bandgap alloy Cu(Ga.In)S₂ led to an inhomogeneous film composition, it is evident that with the use of two SSPs with similar thermal profiles, consistent film stoichiometry might be achieved.

Clearly, the full potential of CuInS₂ photovoltaic devices has not been fully exploited, since the combination of group I-III-VI₂ elements can result in a variety of end products. Therefore standards need to be defined that can associate device processing, fabrication, and film composition to cell bandgap and efficiency. Spray CVD in conjunction with SSP design provides a proof of concept for a highly reproducible manufacturing process. Items that need to be further investigated are

1. Precursor design: More volatile and/or thermally labile systems need to be developed. This can be achieved by the incorporation of fluorinated or silylated functional groups. Importantly, because of the stability of fluorosilyl moieties, incorporation of both elements in the molecule can serve not only to increase volatility but also as a “self-cleaning” mechanism should the precursor not decompose in a desirable pathway.
2. Processing parameters: Spray CVD has a number of tunable variables, such as droplet size, flow rate, concentration, and solvent polarity, which is advantageous to achieve the desired film characteristics. Thus an in-depth study needs to address these parameters with respect to film composition, morphology, and grain structure.
3. Device fabrication: Working devices from deposited films need to be tested to aid SSP design and spray CVD process parameters. The work reported here on the molecular design of SSPs for their use in a spray CVD process, although still in its infancy, undoubtedly shows it as a mass-producible, cost-effective method for fabricating commercial thin-film PV devices.

References

1. Banger, K.K.; Cowen, J.; and Hepp, A.F.: Synthesis and Characterization of the First Liquid Single-Source Precursors for the Deposition of Ternary Chalcopyrite (CuInS_2) Thin Film Materials. *Chem. Mater.*, vol. 13, no. 11, 2001, pp. 3827–3829.
2. Banger, K.K., et al.: Facile Modulation of Single Source Precursors: The Synthesis and Characterization of Single Source Precursors for Deposition of Ternary Chalcopyrite Materials. *Thin Sol. Fi.*, vol. 403, 2002, pp. 390–395.
3. Banger, K.K., et al.: Ternary Single-Source Precursors for Polycrystalline Thin-Film Solar Cells. *Appl. Organomet. Chem.*, vol. 16, no. 11, 2002, pp. 617–627.
4. Banger, K.K., et al.: A New Facile Route for the Preparation of Single-Source Precursors for Bulk, Thin-Film, and Nanocrystallite I–III–VI Semiconductors. *Inorg. Chem.*, vol. 42, no. 24, 2003, pp. 7713–7715.
5. Hollingsworth, J.A., et al.: Ternary Precursors for Depositing I–III–VI₂ Thin Films for Solar Cells Via Spray CVD. *Thin Sol. Fi.*, vols. 431–432, 2003, pp. 63–67.
6. Jin, Michael H., et al.: Thin Film CuInS_2 Prepared by Spray Pyrolysis With Single-Source Precursors. Conference Record of the Twenty-Ninth IEEE Photovoltaic Specialists Conference 2002, IEEE, Piscataway, NJ, 2002, pp. 672–675.
7. Jin, Michael H.–C., et al.: CuInS_2 Films Deposited by Aerosol-Assisted Chemical Vapor Deposition Using Ternary Single-Source Precursors. *Mater. Sci. Eng. B*, vol. 116, no. 3, 2005, pp. 395–401.
8. Kelly, C.V., et al.: Parametric Study on Non-Vacuum Chemical Vapor Deposition of CuInS_2 From a Single-Source Precursor. *Mater. Sci. Eng. B*, vol. 116, no. 3, 2005, pp. 403–408.
9. Jin, Michael H., et al.: Post-Deposition Annealing of Thin Film CuInS_2 Made From a Single-Source Precursor. Conference Record of the 31st IEEE Photovoltaic Specialists Conference, 2005, pp. 382–385.
10. Hoffman, David J., et al.: Thin-Film Photovoltaic Solar Array Parametric Assessment. 17th Space Photovoltaic Research and Technology Conference, NASA/TM—2000-210342 (AIAA—2000–2919), 2000.
11. Contreras, Miguel, et al.: Progress Toward 20% Efficiency in Cu(In,Ga)Se_2 Polycrystalline Thin-Film Solar Cells. *Prog. Photovolt. Res. Appl.*, no. 7, issue 4, 1999, pp. 311–316.
12. Bailey, Sheila G.; and Flood, Dennis J.: Space Photovoltaics. *Prog. Photovolt. Res. Appl.*, vol. 6, issue 1, 1998, pp. 1–14.
13. Schock, Hans-Werner; and Noufi, Rommel: CIGS-Based Solar Cells for the Next Millennium. *Prog. Photovolt. Res. Appl.*, vol. 8, issue 1, 2000, pp. 151–160.
14. Schock, H.W.; and Bogus, K.: Development of CIS Solar Cells for Space Applications. J. Schmid et al., eds., *Proc. 2nd World Conf. on Photovolt. Energy Conv., E.C. Joint Res. Centre, Luxembourg*, 1998, p. 3586.
15. Tarrant, D.; and Ermer, J.: I–III–VI₂ Multinary Solar Cells Based on CuInSe_2 . Conference Record of the 23rd IEEE Photovoltaic Specialists Conference, 1993, pp. 372–378.
16. Klaer, J., et al.: A Tolerant Two Step Process for Efficient CuInS_2 Solar Cells. Proceedings of the 2nd World Conference and Exhibition on Photovoltaic Solar Energy Conversion Conference, Report EUR 18656, Vol. I, European Commission, 1998, pp. 537–540.
17. Ramanathan, K., et al.: Properties of 19.2% Efficiency $\text{ZnO/CdS/CuInGaSe}_2$ Thin-Film Solar Cells. *Prog. Photovolt. Res. Appl.*, vol. 11, no. 4, 2003, pp. 225–230.
18. Archer, Mary D.; and Hill, Robert: *Clean Electricity From Photovoltaics*, ch. 7, Imperial College Press, London, 2001.
19. U.S. Photovoltaic Industry Roadmap. Sandia National Laboratory, 2002. http://photovoltaics.sandia.gov/docs/PVRM_PV_Road_Map.htm Accessed Feb. 20, 2008.
20. Basol, B.M., et al.: Cu(In,Ga)Se_2 Thin Films and Solar Cells Prepared by Selenization of Metallic Precursors. *J. Vac. Sci. Technol. A.*, vol. 14, no. 4, 1996, pp. 2251–2256.
21. Probst, V., et al.: Rapid CIS-Process for High Efficiency PV-Modules: Development Towards Large Area Processing. *Thin Sol. Fi.*, vol. 387, nos. 1–2, 2001, pp. 262–267.
22. Dimmler, B.; and Schock, H.W.: Scalability and Pilot Operation in Solar Cells of CuInSe_2 and Their Alloys. *Prog. Photovolt. Res. Appl.*, vol. 6, no. 3, 1998, pp. 193–199.
23. Park, S.C., et al.: Fabrication of CuInSe_2 Films and Solar Cells by Sequential Evaporation of In_2Se_3 and Cu_2Se Binary Compounds. *Sol. Energy Mater. Sol. Cells*, vol. 69, no. 2, 2001, pp. 99–105.
24. Guillen, C.; and Herrero, J.: Recrystallization and Components Redistribution Processes in Electrodeposited CuInSe_2 Thin Films. *Thin Sol. Fi.*, vol. 387, nos. 1–2, 2001, pp. 57–59.
25. Eberspacher, C., et al.: Thin-Film CIS Alloy PV Materials Fabricated Using Non-Vacuum, Particles-Based Techniques. *Thin Sol. Fi.*, vol. 387, nos. 1–2, 2001, pp. 18–22.
26. Klenk, M., et al.: Properties of Flash Evaporated Chalcopyrite Absorber Films and Solar Cells. *Thin Sol. Fi.*, vol. 387, nos. 1–2, 2001, pp. 47–49.
27. Dzionk, C., et al.: Phase Formation During the Reactive Annealing of Cu-In Films in H_2S Atmosphere. *Thin Sol. Fi.*, vol. 299, nos. 1–2, 1997, pp. 38–44.
28. Krunks, M., et al.: Composition and Structure of CuInS_2 Films Prepared by Spray Pyrolysis. *Thin Sol. Fi.*, vol. 361, 2000, pp. 61–64.
29. Artaud, M.C., et al.: CuInSe_2 Thin Films Grown by MOCVD: Characterization, First Devices. *Thin Sol. Fi.*, vol. 324, nos. 1–2, 1998, pp. 115–123.
30. Jones, Anthony C.; and O'Brien, Paul: *CVD of Compound Semiconductors: Precursors Synthesis, Development and Applications*. VCH Press, Weinheim, 1997.
31. Rees, William S.: *CVD of Nonmetals*. VCH Press, Weinheim, 1996.
32. Keys, A., et al.: Tert-Butyl Compounds of Gallium. *J. Chem. Soc. (London) Dalton Trans.*, vol. 4, 2000, pp. 577–588.
33. Gleizes, A.N.: MOCVD of Chalcogenides, Pnictides, and Heterometallic Compounds From Single-Source Molecule Precursors. *Chem. Vap. Deposition*, vol. 6, no. 4, 2000, pp. 155–173.
34. Kodas, Toivo T.; and Hampden-Smith, Mark J., eds.: *The Chemistry of Metal CVD*. VCH, Weinheim, 1994.
35. Nomura, Ryoki; Kanaya, Kouichi; and Matsuda, Haruo: Preparation of Copper-Indium-Sulfide Thin Films by Solution Pyrolysis of Organometallic Sources. *Chem. Lett.*, vol. 17, no. 11, 1988, pp. 1849–1850.
36. Nomura, R., et al.: Oxygen-Containing or Sulfur-Containing Organoindium Compounds for Precursors of Indium Oxide and Sulfide Thin-Films. *PLYHD.*, vol. 9, nos. 2–3, 1990, pp. 361–366.

37. Nomura, R.; Seki, Y.; and Matsuda, H.: Preparation of CuInS_2 Thin-Films by Single-Source MOCVD Process Using $\text{Bu}_2\text{In}(\text{SPr})\text{Cu}(\text{S}_2\text{CNPr}_2)$. *J. Mater. Chem.*, vol. 2, no. 7, 1992, pp. 765–766.
38. Nomura, R.; Seki, Y.; and Matsuda, H.: Preparation of CuIn_5S_8 Thin Films by Single-Source Organometallic Chemical Vapor-Deposition. *Thin Sol. Fi.*, vol. 209, no. 2, 1992, pp. 145–147.
39. Hirpo, Wakgari, et al.: Synthesis of Mixed Copper-Indium Chalcogenolates. Single-Source Precursors for the Photovoltaic Materials CuInQ_2 (Q = S, Se). *J. Am. Chem. Soc.*, vol. 115, no. 4, 1993, pp. 1597–1599.
40. Hollingsworth, J.A.; Hepp, A.F.; and Buhro, W.E.: Spray CVD of Copper Indium Disulfide Films: Control of Microstructure and Crystallographic Orientation. *Chem. Vap. Deposition*, vol. 5, no. 3, 1999, pp. 105–108.
41. Hollingsworth, J.A., et al.: Spray Chemical Vapor Deposition of CuInS_2 Thin Films for Application in Solar Cell Devices. *Chemical Aspects of Electronic Ceramics Processing Symposium*, P.N. Kumta et. al., eds., Materials Research Society, Warrendale, PA, 1998, pp. 171–176.
42. Harris, J.D., et al.: Using Single Source Precursors and Spray Chemical Vapor Deposition to Grow Thin-Film CuInS_2 . *Proceedings of the 28th IEEE Photovoltaic Specialists Conference*, IEEE, Piscataway, NJ, 2000, pp. 563–566.
43. Cowen, J.E., et al.: Synthesis and Characterization of CuInS_2 Single Source Precursors for Chemical Vapor Deposition. *J. Therm. Analysis Calor.*, vol. 75, no. 3, 2004, pp. 929–935.
44. Miyake, H.; Hayashi, T.; and Sugiyama, K.: Preparation of $\text{CuGa}_x\text{In}_{1-x}\text{S}_2$ Alloys From In Solutions. *J. Cryst. Growth.*, vol. 134, nos. 3–4, 1993, pp. 174–180.
45. The International Centre for Diffraction Data Mission and Vision. ICDD, <http://www.icdd.com/>. Accessed April 29, 2008.
46. Shaukat, A.: Composition-Dependent Band-Gap Variation of Mixed Chalcopyrites. *J. Phys. Chem. Solids*, vol. 51, no. 12, 1990, pp. 1413–1418.
47. Odier, P., et al.: Spray Pyrolysis for High T_c Superconductor Films. *Supercond. Sci. Technol.*, vol. 17, no. 11, 2004, pp. 1303–1310.
48. Krumdieck, S.; Sbaizero, O.; and Raj, R.: Unique Precursor Delivery and Control Afforded by Low-Pressure Pulsed-CVD Process With Ultrasonic Atomization. *J. Phys. IV*, vol. 11, 2001, pp. 1161–1168.
49. Zhang, S.B., et al.: Defect Physics of the CuInS_2 Chalcopyrite Semiconductor. *Phys. Rev. B*, vol. 57, no. 16, 1998, pp. 9642–9656.
50. Harris, J.D., et al.: Characterization of CuInS_2 Films Prepared by Atmospheric Pressure Spray Chemical Vapor Deposition. *Mater. Sci. Eng. B*, vol. 98, no. 2, 2003, pp. 150–155.
51. Albin, D., et al.: Composition-Structure Relationships for Multisource Evaporated (CuGaSe_2) Thin Films. *J. Appl. Phys.*, vol. 64, no. 10, pt. 1, 1988, pp. 4903–4908.
52. Edington, Jeffrey W.: *Practical Electron Microscopy in Materials Science*. Van Nostrand Reinhold Co., New York, NY, 1976.
53. Soliman, H.S.: Structural and Optical Properties of Thin Films of CuGaS_2 . *J. Phys. D Appl. Phys.*, vol. 31, no. 13, 1998, pp. 1516–1521.
54. Scheer, R.; Diesner, K.; and Lewerenz, H.J.: Experiments on the Microstructure of Evaporated CuInS_2 Thin Films. *Thin Sol. Fi.*, vol. 268, nos. 1–2, 1995, pp. 130–136.
55. Tell, B.; Shay, J. L.; and Kasper, H.M.: Room-Temperature Electrical Properties of 10 I–III–VI₂ Semiconductors. *J. Appl. Phys.*, vol. 43, no. 5, 1972, pp. 2469–2470.
56. Tiller, W.A.: Dendrites. Understanding of This Familiar Phenomenon Has Led to the Development of Useful Man-Made Materials. *SCI.*, no. 3646, vol. 146, 1964, pp. 871–879.
57. Jaffe J.E.; and Zunger, A.: Anion Displacements and the Band-Gap Anomaly in Ternary ABC_2 Chalcopyrite Semiconductors. *Phys. Rev. B: Condens. Matter*, vol. 28, no. 8, 1983, pp. 5176–5179.
58. Jokanovic, V., et al.: Modeling of Nanostructural Design of Ultrafine Mullite Powder Particles Obtained by Ultrasonic Spray Pyrolysis. *Nanostruct. Mater.*, vol. 12, nos. 1–4, 1999, pp. 349–352.
59. Kodas, Toivo T.; and Hampden-Smith, Mark J.: *Aerosol Processing of Materials*. Ch. 5, Wiley-VCH, New York, NY, 1999.
60. Jin, M.H., et al.: Thin Film CuInS_2 Prepared by Spray Pyrolysis With Single-Source Precursors. *Conference Record of the 29th IEEE Photovoltaic Specialists Conference*, IEEE, Piscataway, NJ, 2002, pp. 672–675.
61. Álvarez-García, J., et al.: Microstructure and Secondary Phases in Coevaporated CuInS_2 Films: Dependence on Growth Temperature and Chemical Composition. *J. Vac. Sci. Technol. A*, vol. 19, no. 1, 2001, pp. 232–239.
62. Weber, M., et al.: Microroughness and Composition of Cyanide-Treated CuInS_2 . *J. Electrochem. Soc.*, vol. 149, no. 1, 2000, pp. G77–G84.
63. Look, D.C.; and Manthuruthil, J.C.: Electron and Hole Conductivity in CuInS_2 . *J. Phys. Chem. Solids*, vol. 37, no. 2, 1976, pp. 173–180.
64. Kazmerski, L.L.; Ayyagari, M.S.; and Sandborn, G.A.: CuInS_2 Thin Films: Preparation and Properties. *J. Appl. Phys.*, vol. 46, no. 11, 1975, pp. 4865–4869.
65. Van den Brekel, C.H.J.: Characterization of Chemical Vapour-Deposition Processes. I. *Philips Res. Rep.*, vol. 32, no. 2, 1977, pp. 118–133.
66. Siemer, K., et al.: Influence of Crystal Orientation on Device Performance of CuInS_2 Solar Cells. *Proceedings of the 28th IEEE Photovoltaic Specialists Conference*, IEEE, Piscataway, NJ, 2000, pp. 630–633.
67. Siebentritt, S.: Wide Gap Chalcopyrites: Material Properties and Solar Cells. *Thin Sol. Fi.*, vols. 403–404, 2002, pp. 1–8.
68. Ueng, H.Y.; and Hwang, H.L.: The Defect Structure of CuInS_2 . I. Intrinsic Defects. *J. Phys. Chem. Solids*, vol. 50, no. 12, 1989, pp. 1297–1305.
69. Gossia, M.; Metzner, H.; and Mahnke, H.-E.: CuInS_2 Thin-Films From Co-Evaporated Precursors. *Thin Sol Fi.*, vol. 387, nos. 1–2, 2001, 2001, pp. 77–79.
70. Topper, K., et al.: Photoluminescence of CuInS_2 Thin Films and Solar Cells Modified by Postdeposition Treatments. *Appl. Phys. Lett.*, vol. 71, no. 4, 1997, pp. 482–484.
71. Leite, R.C.C.; and DiGiovanni, A.E.: Frequency Shift With Temperature as Evidence for Donor-Acceptor Pair Recombination in Relatively Pure n-Type GaAs. *Phys. Rev.*, vol. 153, no. 3, 1967, pp. 841–843.
72. Binsma, J.J.M.; Giling, L.J.; and Bloem, J.: Luminescence of CuInS_2 . I. The Broad Band Emission and Its Dependence on the Defect Chemistry. *J. Luminesc.*, vol. 27, no. 1, 1982, pp. 35–53.

73. Binsma, J.J.M.; Giling, L.J.; and Bloem, J.: Luminescence of CuInS₂. II. Exciton and Near Edge Emission. *J. Luminesc.*, vol. 27, no. 1, 1982, pp. 55–72.
74. Ueng, H.Y.; and Hwang, H.L.: The Defect Structure of CuInS₂. Part II: Thermal Annealing Defects. *J. Phys. Chem. Solids*, vol. 51, no. 1, 1990, pp. 1–10.
75. Schon, J.H.; and Bucher, E.: Characterization of Intrinsic Defect Levels in CuInS₂. *Phys. Stat. Sol. A.*, vol. 171, no. 2, pp. 511–519.
76. Krustok, J., et al.: The Role of Deep Donor-Deep Acceptor Complexes in CIS-Related Compounds. *Thin Sol. Fi.*, vols. 361–362, 2000, pp. 406–410.
77. Nanu, M.; Schoonman, J.; and Goossens, A.: Raman and PL Study of Defect-Ordering in CuInS₂ Thin Films. *Thin Sol. Fi.*, vols. 451–452, 2004, pp. 193–197.
78. Hanket, G.M., et al.: Fabrication of Graded Cu(InGa)Se₂ Films by Inline Evaporation. *Proceedings of the 28th IEEE Photovoltaic Specialists Conference*, IEEE, Piscataway, NJ, 2000, pp. 499–504.

Glenn Research Center
National Aeronautics and Space Administration
Cleveland, Ohio, November 24, 2008.

REPORT DOCUMENTATION PAGE

Form Approved
OMB No. 0704-0188

The public reporting burden for this collection of information is estimated to average 1 hour per response, including the time for reviewing instructions, searching existing data sources, gathering and maintaining the data needed, and completing and reviewing the collection of information. Send comments regarding this burden estimate or any other aspect of this collection of information, including suggestions for reducing this burden, to Department of Defense, Washington Headquarters Services, Directorate for Information Operations and Reports (0704-0188), 1215 Jefferson Davis Highway, Suite 1204, Arlington, VA 22202-4302. Respondents should be aware that notwithstanding any other provision of law, no person shall be subject to any penalty for failing to comply with a collection of information if it does not display a currently valid OMB control number.

PLEASE DO NOT RETURN YOUR FORM TO THE ABOVE ADDRESS.

1. REPORT DATE (DD-MM-YYYY) 01-11-2008		2. REPORT TYPE Technical Paper		3. DATES COVERED (From - To)	
4. TITLE AND SUBTITLE Spray Chemical Vapor Deposition of Single-Source Precursors for Chalcopyrite I-III-VI ₂ Thin-Film Materials				5a. CONTRACT NUMBER	
				5b. GRANT NUMBER	
				5c. PROGRAM ELEMENT NUMBER	
6. AUTHOR(S) Hepp, Aloysius, F.; Banger, Kulbinder, K.; Jin, Michael, H.-C.; Harris, Jerry, D.; McNatt, Jeremiah, S.; Dickman, John, E.				5d. PROJECT NUMBER	
				5e. TASK NUMBER	
				5f. WORK UNIT NUMBER WBS 953033.01.03.23	
7. PERFORMING ORGANIZATION NAME(S) AND ADDRESS(ES) National Aeronautics and Space Administration John H. Glenn Research Center at Lewis Field Cleveland, Ohio 44135-3191				8. PERFORMING ORGANIZATION REPORT NUMBER E-16162-1	
9. SPONSORING/MONITORING AGENCY NAME(S) AND ADDRESS(ES) National Aeronautics and Space Administration Washington, DC 20546-0001				10. SPONSORING/MONITORS ACRONYM(S) NASA	
				11. SPONSORING/MONITORING REPORT NUMBER NASA/TP-2008-214937	
12. DISTRIBUTION/AVAILABILITY STATEMENT Unclassified-Unlimited Subject Categories: 25 and 44 Available electronically at http://gltrs.grc.nasa.gov This publication is available from the NASA Center for AeroSpace Information, 301-621-0390					
13. SUPPLEMENTARY NOTES Based upon chapter to be published in "Solution-Based Processing of Inorganic Films," edited by David Mitzi of IBM and published by John Wiley and Sons Scientific, Technical, and Medical Publishing, Hoboken, New Jersey.					
14. ABSTRACT Thin-film solar cells on flexible, lightweight, space-qualified substrates provide an attractive approach to fabricating solar arrays with high mass-specific power. A polycrystalline chalcopyrite absorber layer is among the new generation of photovoltaic device technologies for thin film solar cells. At NASA Glenn Research Center we have focused on the development of new single-source precursors (SSPs) for deposition of semiconducting chalcopyrite materials onto lightweight, flexible substrates. We describe the syntheses and thermal modulation of SSPs via molecular engineering. Copper indium disulfide and related thin-film materials were deposited via aerosol-assisted chemical vapor deposition using SSPs. Processing and post-processing parameters were varied in order to modify morphology, stoichiometry, crystallography, electrical properties, and optical properties to optimize device quality. Growth at atmospheric pressure in a horizontal hot-wall reactor at 395 °C yielded the best device films. Placing the susceptor closer to the evaporation zone and flowing a more precursor-rich carrier gas through the reactor yielded shinier-, smoother-, and denser-looking films. Growth of (112)-oriented films yielded more Cu-rich films with fewer secondary phases than growth of (204)/(220)-oriented films. Post-deposition sulfur-vapor annealing enhanced stoichiometry and crystallinity of the films. Photoluminescence studies revealed four major emission bands and a broad band associated with deep defects. The highest device efficiency for an aerosol-assisted chemical vapor deposited cell was one percent.					
15. SUBJECT TERMS Vapor deposition; Thin films; Solar cells; Synthesis (chemistry); Inorganic sulfides; Thermal analysis; X-ray diffraction; Photoluminescence; Scanning electron microscopy					
16. SECURITY CLASSIFICATION OF:			17. LIMITATION OF ABSTRACT UU	18. NUMBER OF PAGES 32	19a. NAME OF RESPONSIBLE PERSON STI Help Desk (email:help@sti.nasa.gov)
a. REPORT U	b. ABSTRACT U	c. THIS PAGE U			19b. TELEPHONE NUMBER (include area code) 301-621-0390

